NASA Technical Paper 3476

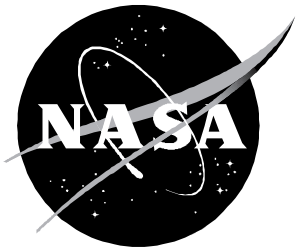

Internal Aerodynamics of a Generic Three-Dimensional Scramjet Inlet at Mach 10

Scott D. Holland

January 1995

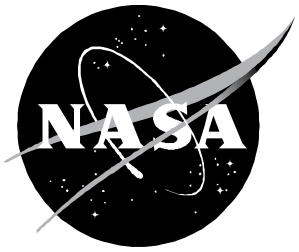

NASA Technical Paper 3476

Internal Aerodynamics of a Generic Three-Dimensional Scramjet Inlet at Mach 10

Scott D. Holland
Langley Research Center • Hampton, Virginia

National Aeronautics and Space Administration
Langley Research Center • Hampton, Virginia 23681-0001

January 1995

The use of trademarks or names of manufacturers in this report is for accurate reporting and does not constitute an official endorsement, either expressed or implied, of such products or manufacturers by the National Aeronautics and Space Administration.

This publication is available from the following sources:

NASA Center for AeroSpace Information
800 Elkridge Landing Road
Linthicum Heights, MD 21090-2934
(301) 621-0390

National Technical Information Service (NTIS)
5285 Port Royal Road
Springfield, VA 22161-2171
(703) 487-4650

Contents

Summary

A combined experimental and computational parametric study of the internal aerodynamics of a generic three-dimensional sidewall compression scramjet inlet configuration at Mach 10 has been performed. The study was designed to demonstrate the utility of computational fluid dynamics (CFD) as a design tool in hypersonic inlet flow fields, to examine the nature and structure of the flow interactions inside an inlet subject to a high Mach number laminar inflow, and to provide a comprehensive surface property and flow field database of the effects of contraction ratio, cowl position, and Reynolds number on the performance of a hypersonic scramjet inlet configuration. The work proceeded in several phases: the initial inviscid assessment of the internal shock structure, the preliminary computational parametric study, the coupling of the optimized configuration with the physical limitations of the facility, the wind tunnel blockage assessment, and the experimental and computational parametric study of the final configuration.

An initial inviscid assessment was performed by appropriately modifying inviscid two-dimensional oblique shock theory to accommodate the three-dimensional effects of leading-edge sweep. This modification demonstrated that the principal effect of leading-edge sweep was the introduction of a downward component to the flow aft of the internal swept shocks. When the cowl is fully retracted, this downturned flow spills out of the inlet. This spillage is important in helping the inlet start at lower Mach numbers. As the Mach number is increased, the sidewall shock angles become smaller, effectively reducing the spillage window and increasing the mass capture. These variable geometry characteristics make it possible to consider a fixed geometry inlet for use over a wide Mach number range.

A preliminary computational parametric study was then performed using the three-dimensional Navier-Stokes code SCRAMIN to identify inlet characteristics pertinent to the optimization of the configuration for a Mach 10 inflow. The primary interest was the variation of the performance parameters of mass capture, throat Mach number, total pressure recovery (and hence kinetic energy efficiency), and internal compression with leading-edge sweep. The results of the trade study led to the selection of a 45° leading-edge sweep configuration for further computational and experimental evaluation.

Following a brief experimental wind tunnel blockage study (which found no evidence of tunnel blockage), a highly instrumented wind tunnel model was fabricated. A total of 256 channels of pressure data, including static pressure orifices, pitot pressures, and entrance and exit flow rakes, along with oil flow and infrared thermography, provided a detailed experimental description of the internal flow characteristics. Mach 10 experiments were performed for three geometric contraction ratios (3, 5, and 9), three Reynolds numbers (0.55×10^6 per foot, 1.14×10^6 per foot, and 2.15×10^6 per foot), and three cowl positions (cowl at throat and at two forward positions). For contraction ratios (CR) of 5 and 9, a large forward separation of the inflow boundary layer was observed. A decrease in Reynolds number (Re) from 2.15×10^6 per foot to 1.14×10^6 per foot for all three contraction ratios yielded similar results. Only the CR = 3 configuration at Re = 2.15×10^6 per foot was observed to operate "on design," for which the dominant effect of forward cowl placement was observed to be decreased spillage. Computational results were obtained for CR = 3 at a unit free-stream Reynolds number of 2.15×10^6 per foot for two cowl positions; good quantitative agreement was obtained between computation and experiment for these configurations.

Symbols

$C_{x'}$	distance from cowl leading edge to throat entrance, in.
CR	geometric contraction ratio, W/g
g	throat gap, in.
H	height of inlet, 4.0 in.
i	axial grid coordinate index
M_1	free-stream Mach number
M_e	Mach number at edge of boundary layer
p	static pressure, psia
$p_{t,1}$	tunnel stagnation pressure, psia
$p_{t,2}$	pitot pressure, psia
p_∞	free-stream static pressure, psia
Re	free-stream Reynolds number
Re_θ	Reynolds number based on momentum thickness
T	static temperature, °R
$T_{t,1}$	tunnel stagnation temperature, °R
$T_{x'}$	distance from sidewall leading edge to throat, 9.5 in.
W	inlet width at sidewall leading edge, in.

x	axial distance measured from baseplate leading edge, in.
x'	local axial distance measured from sidewall leading edge, in.
y	lateral distance across baseplate, measured from centerline toward sidewall, in.
y_{wall}	local distance from centerline to wall, in.
Z	vertical distance from baseplate, defined for convenience positive *down* sidewall toward cowl, in.
z	vertical distance from baseplate, measured to complete right-hand set, in.
γ	ratio of specific heats
δ	sidewall compression angle, deg
Λ	leading-edge sweep angle, deg

Introduction

Recent programs have refocused attention on the attractive potential of hypersonic flight. High Mach number propulsion for airbreathing vehicles such as the National Aero-Space Plane (X-30) is planned to be accomplished with supersonic combustion ramjets (refs. 1–3). According to Kandebo (ref. 4), the restructured NASP program (HYFLITE, HySTP) includes plans to flight-test hydrogen-fueled scramjets. The advantages of an airframe integrated propulsion system for increased efficiency have been well recognized for many years (ref. 5). This concept (see fig. 1) makes use of the forebody bow shock, which precompresses the flow upstream of the inlet entrance. Because an inlet would be limited by the dimensions of the shock layer, and because the inlet should process a maximum amount of the oncoming stream, this concept necessarily requires ingestion of the forebody boundary layer. One inlet concept which has been the subject of study for many years makes use of wedge-shaped sidewalls to obtain further compression in the horizontal direction, reducing the total inplane turning the flow must encounter to obtain the desired compression. The sidewall leading edges are swept both to reduce the aerothermal loads on the leading edges and to promote spillage at the lower Mach numbers to aid in starting the inlet. The sweep has the effect of turning the flow away from the forebody plane, leading to a decrease in mass capture due to flow spillage ahead of the cowl. As the Mach number is increased, the sidewall shock angles become smaller, reducing the spillage window and increasing the mass capture. These characteristics make it possible to consider a fixed geometry inlet for use over a wide Mach number range.

Much of the early work on three-dimensional sidewall compression scramjet inlet concepts has been performed by Trexler and colleagues. Trexler (ref. 6) presented a brief summary of Mach 6 survey data in the inlet region of the Langley Integrated Scramjet Module. A more complete data set was later presented over a Mach number range of 2.3 to 6.0 for the same integrated scramjet module (ref. 7). Boundary-layer trips on the foreplate provided the inlet with a thick turbulent boundary layer, simulating the vehicle forebody boundary layer. The low-pressure gradient on this surface (i.e., no ramp compression on this surface) was found to permit ingestion of this boundary layer without separation. The sweep of the sidewall compression surfaces provided a mechanism for spillage to allow the inlet to start at low Mach numbers. The added drag due to this spillage was not determined, but it was noted that the spillage would augment the lift because it turns the flow in a downward direction. Struts were located in the inlet throat region to provide a means to introduce fuel and to aid in the compression process. Trexler and Souders (ref. 8) presented wall static pressure distributions, oil flow data, wall surface temperature measurements, pitot surveys, and gross performance parameters for a detailed evaluation of a baseline inlet configuration. It was demonstrated that at a Mach number of 6, the inlet (with an average contraction ratio of 7) would start and that starting was enhanced by the downturning due to the sidewall sweep, that the inlet capture and kinetic energy efficiency were acceptable (94 and 97.7 percent, respectively), and that the forebody boundary layer could be ingested with no adverse effects. Although the Mach number was lower than the present work and the boundary layer was turbulent, these works illustrate the complexity of the fundamental shock interactions in the sidewall compression inlet.

Holland and Perkins (ref. 9) and Holland and Murphy (ref. 10) reported on Mach 6 testing of three-dimensional sidewall compression scramjet inlets with leading-edge sweep angles of 30° and 70° in tetrafluoromethane and air, respectively. By testing in both tetrafluoromethane ($\gamma = 1.2$) and air ($\gamma = 1.4$), the explicit effects of the ratio of specific heats (and hence the normal shock density ratio) could be obtained. It is recognized that the simulation of so-called "real gas" effects is approximate, due to the variation of ratio of specific heats about a slender body in flight compared with the relatively

constant γ obtained in tetrafluoromethane. Nevertheless, the effects of high-temperature gas could be approximated (bounded) by testing in these test gases. It was found that a decrease in ratio of specific heats (as may be observed at higher flight Mach numbers) did not increase sensitivity to unstart.

There also appears to have been recent foreign interest in three-dimensional inlet configurations similar to the Langley Integrated Scramjet Module. Vinogradov et al. (ref. 11) reported on numerical and experimental work in the USSR for inlets with and without struts at Mach numbers between 2 and 6. They found that their fixed geometry inlet with swept compression surfaces started in the Mach 1.8 to 2.1 range and exhibited performance characteristics better than those obtained for fixed geometry two-dimensional inlets. They also showed good agreement between computation and experiment for the greater part of the inlet flow field. Kanda et al. (ref. 12) reported on work done in Japan at Mach 4 on six inlet configurations based on the Langley inlet. Schlieren photographs of the flow beneath the model indicated the presence of flow downturning (mass spillage). They compared total pressure recovery and mass capture at Mach 4 for leading-edge sweeps of 30°, 45°, and 60°; their results indicated a slight increase in total pressure recovery and mass capture between 30° and 45° and a significant decrease in both parameters at 60°. They therefore report a sweep angle of 45° as best for Mach 4 operation. In addition to the experimental work, they made approximate calculations of the pressure field through the use of the two-dimensional oblique shock relations. They also employed a two-dimensional Navier-Stokes code, which they concluded was useful, but due to the strong three-dimensional nature of the flow field, a full three-dimensional code was required.

Considerable computational and experimental effort has been made to examine the fundamental flow physics for the more general problem of shock/boundary-layer interactions in single and double fin configurations. Settles and Dolling (refs. 13 and 14) have presented complete reviews of the experimental, analytical, and computational research on three-dimensional sharp fin interactions. Most of the research has examined turbulent-boundary-layer interactions at supersonic Mach numbers. For example, Knight et al. (ref. 15) compared computational and experimental results for a sharp fin/turbulent-boundary-layer interaction at Mach 4, Reddy (ref. 16) presented computational results for a crossing shock/turbulent-boundary-layer interaction at Mach 3.5 and 4.0, and Narayanswami (ref. 17) numerically examined the interaction between crossing oblique shocks and a turbulent boundary layer at both Mach 2.95 and 8.2.

White et al. (ref. 18) point out the utility of computational fluid dynamics (CFD) for providing parametric studies in a timely and cost-effective manner, and once wind tunnel data are obtained, to aid in the explanation of unusual or unexpected phenomena by giving detailed flow field data. The present work uses CFD in this design and analysis capacity. The three-dimensional Navier-Stokes code SCRAMIN of Kumar (ref. 19) was chosen for this study because it uses the well-known and well-proven MacCormack's explicit predictor-corrector numerical scheme (ref. 20) and has shown favorable comparison with experiment at Mach numbers between 2 and 6. Because instrumented wind tunnel models are quite expensive, CFD has been utilized to minimize the costs of fabrication by eliminating from consideration designs which promise poor performance.

A preliminary computational parametric study was performed to examine the variation of the performance parameters of mass capture, throat Mach number, total pressure recovery (and hence kinetic energy efficiency), and internal compression with leading-edge sweep for a laminar, Mach 10 inflow. The configuration of the Mach 2 to 6 computations (see fig. 8 of ref. 21) was adopted for this initial parametric study. The results of the trade study (ref. 22) led to the selection of a 45° leading-edge sweep configuration for further computational and experimental evaluation.

Following a wind tunnel blockage study (ref. 23), a highly instrumented wind tunnel model was fabricated and tested in the Langley 31-Inch Mach 10 Tunnel. A total of 256 channels of pressure data, including static pressure orifices, free-stream pitot pressures, and entrance and exit flow rakes, along with oil flow and infrared thermography provided a detailed experimental description of the flow for comparison with computation. Experimental tests were performed for three geometric contraction ratios (3, 5, and 9), three Reynolds numbers (0.55×10^6 per foot, 1.14×10^6 per foot, and 2.15×10^6 per foot), and three cowl positions (cowl at throat and at two forward positions). Computational results were obtained for CR = 3 at Re = 2.15×10^6 per foot for two cowl positions. The experimental and computational data sets have been released in the companion documents, references 24 and 25, respectively.

The present work summarizes the results of a combined computational and experimental parametric investigation of the internal aerodynamics

of a generic three-dimensional sidewall compression scramjet inlet at Mach 10 (ref. 26). Although geometrically simple, inlets of this genre generate a very complicated flow field, in which corner flow, shock-induced separation, and shock-shock/shock-boundary-layer interactions are among the flow characteristics. Each of these issues have been addressed separately by other researchers, but the desired result from the inlet is the creation of a nearly uniform, supersonic, compressed flow at the inlet exit. The prediction of such complicated flow fields is of particular interest to vehicle designers and analysts for whom high local pressure gradients and high heating influence the total aerodynamic and structural design of the flight vehicle.

The goals of the combined numerical and experimental investigation are threefold: to demonstrate the utility of computational fluid dynamics as a design tool in hypersonic inlet flow fields, to examine the nature and structure of the flow interactions inside an inlet subject to a high-Mach-number laminar inflow, and to provide a comprehensive surface property and flow field database to determine the effects of contraction ratio, cowl position, and Reynolds number on the performance of a hypersonic scramjet inlet configuration. Computational fluid dynamics is used to drive the design of the experimental configuration; the experimental work is in turn used to provide a validation for the computational parametrics.

Experimental Techniques

Model Description

The leading-edge sweep (Λ) and the sidewall compression angle (δ) were fixed at 45° and 6°, respectively. (See sketch, fig. 2.) The model was injected into the tunnel in flight orientation, with the cowl on the bottom. The forebody plane was represented by a flat plate, which extended 9 in. ahead of the inlet entrance plane. (See the dimensioned drawing, fig. 3.) The inlet sidewalls were 4.0 in. tall with a total length of 21 in. The sidewalls were mounted on a 30-in.-long flat plate (referred to as the baseplate) which provided the inflow laminar boundary layer. The model was designed to maintain a nearly constant wall temperature over the course of the short run time. This was accomplished by fabricating the model of oxygen-free high conductivity (OFHC) copper to allow for rapid conduction of heat away from the sharp leading edges and by insulating the outboard sides of the sharp leading edges with zirconium oxide. Over the first 2 sec of run time, infrared thermography results showed that the surface temperature rose by a maximum of only 30 K at the leading edge and 3 K at 1.5 in. downstream of the leading edge ($x'/T_{x'} \approx -0.75$) (fig. 4) for Re $= 2.15 \times 10^6$ per foot. Pitot probes at the same axial location as the baseplate leading edge (as shown in fig. 3), along with settling chamber pressure and temperature, provided tunnel flow conditions. An 11-probe rake was placed outboard of the inlet at the same axial location as the entrance plane (i.e., 9 in. aft of the baseplate leading edge); the exit plane was traversed by an 11-probe core flow rake and a 7-probe boundary-layer rake. A photograph of the inlet model is presented in figure 5.

The geometric contraction ratio, the ratio of the inlet entrance width to the throat gap, W/g (see fig. 2), can be varied by laterally bringing the sidewalls closer together. (Contraction ratios of 3, 5, and 9 were tested; table I provides the respective values of W and g for each contraction ratio.) To prevent covering numerous orifices concentrated in the sidewall/baseplate corner region when moving the sidewalls closer together, it was deemed more efficient to fix one sidewall and heavily instrument that corner. An increase in contraction ratio was accomplished by repositioning the movable sidewall. Although this has the disadvantage of having three effective centerlines, it minimizes the number of orifices covered (and hence rendered useless) when the contraction ratio is increased. Static pressure orifices were oriented such that effective centerline pressure distributions could be obtained for each contraction ratio. Pressure orifices located in lateral arrays provided the horizontal pressure distribution at 25 axial stations between the leading edge of the baseplate and the exit of the inlet throat (fig. 6). Because approximate inviscid analysis suggests shock interactions and impingements occur along lines of constant sweep, vertical arrays of orifices on the sidewalls were swept at the leading-edge sweep angle (fig. 7). The centerline of the cowl was also instrumented with 15 static pressure orifices.

Table I. Inlet Entrance and Throat Gaps for Each Contraction Ratio

CR	W	g
3	3.00	1.00
5	2.50	.50
9	2.25	.25

The cowl position was defined by the forward extent of the cowl leading edge ahead of the throat entrance ($C_{x'}$, see fig. 7) as a percentage of the

distance between the sidewall leading edge and the throat entrance ($T_{x'}$). Thus, when the cowl was moved forward halfway between the beginning of the throat and the sidewall leading edge, it was termed "50 percent cowl" ($C_{x'}/T_{x'} = 0.50$). Likewise, when the cowl was forward of the throat by one-quarter of the distance between the throat and the sidewall leading edge, it was termed "25 percent cowl" ($C_{x'}/T_{x'} = 0.25$). Finally, when the cowl was located at the throat entrance, it was termed "0 percent cowl" ($C_{x'}/T_{x'} = 0$).

Description of Wind Tunnel Facility

The facility used for the present work was the Langley 31-Inch Mach 10 Tunnel. A brief outline of the tunnel performance characteristics can be found in reference 27; a lengthier discussion, in reference 28. The test gas, dry air, is heated to a nominal temperature of 1850°R by a 12.5-MW electrical resistance heater to prevent air liquefaction in the 31- by 31-in. square test section. The maximum reservoir pressure is approximately 1500 psia. The settling chamber, nozzle, throat, test section, adjustable second minimum, and subsonic diffuser are all water cooled. The Langley 31-Inch Mach 10 Tunnel is the only hypersonic facility in the United States to have a three-dimensional contoured nozzle (ref. 29), and due to its three-dimensional contoured design the facility is free of the centerline disturbance characteristically observed in axisymmetric contoured nozzles. Primarily because of this highly uniform core flow, Miller (ref. 30) identified this facility as particularly attractive for CFD computer code calibration studies.

The model is supported on a hydraulically operated, sidewall-mounted injection system capable of injecting the model to centerline in less than 0.6 sec. Prior to injection, the model is stored in a housing which is isolated from the test section by a sliding door. This enclosure rotates about a vertical axis to provide access to the model. Though somewhat inconvenient in that it blocks the optical path for the schlieren, this sidewall-mounted rotating arrangement was designed to allow access to the model without opening the test section to atmosphere so that model changes could be made easily without having to shut down the tunnel when it was operated in continuous mode (fig. 8).

Test Conditions and Test Matrix

Nominal test conditions for the present test were chosen to provide as large a range of Reynolds numbers as possible and to coincide with conditions for which previous facility calibrations had been performed. Tests were performed at Mach 10 for reservoir pressures of 1450, 720, and 350 psia at a reservoir temperature of 1850°R. This yielded free-stream unit Reynolds numbers of 2.15, 1.14, and 0.55×10^6 per foot, respectively. Free-stream static pressures were quite low: 0.03 psia, 0.016 psia, and 0.009 psia, respectively. Generally the pitot pressure at the test section is not obtained during the run because of the orientation of the injection system and location of the model in the facility. Thus, the test section flow conditions were obtained using measured values of reservoir pressure p_{t1}, temperature T_{t1}, and the results of an unpublished calibration. As discussed in reference 31, the computation of free-stream conditions is performed accounting for imperfect gas effects in the reservoir and assuming an isentropic expansion from the reservoir to the test section. The present model did, however, have pitot probes to measure the free-stream pitot pressure, but because the measured pressures agreed with the facility calibration within the accuracy of the measurement, the procedure to calculate free-stream conditions remained unmodified.

Holland et al. (ref. 23) performed an experimental wind tunnel blockage study to determine the effect of the size of the model on the performance of the facility. Despite the fact that the maximum cross-sectional area of the model exceeded 30 percent of the inviscid test core, no evidence of tunnel blockage was noted, based on both pitot pressure measurements of the free stream and static pressure measurements along the tunnel sidewall.

The test matrix was then constructed to examine three principle parametric variables: contraction ratio, cowl position, and Reynolds number. Each of these variables has 3 nominal values, yielding a total of 27 configurations to be tested. Run numbers are provided in tables II, III, and IV for free-stream unit Reynolds numbers per foot of 0.55×10^6, 1.14×10^6, and 2.15×10^6, respectively. (Configurations having more than one run number were used as a check on repeatability.)

Table II. Test Matrix (Runs) for Re = 0.55×10^6 Per Foot

CR	Run number at—		
	0 percent cowl	25 percent cowl	50 percent cowl
3	64	61	58
5	44	41	37, 38
9	47	50	55

Table III. Test Matrix (Runs) for Re = 1.14×10^6 Per Foot

CR	Run number at—		
	0 percent cowl	25 percent cowl	50 percent cowl
3	65, 67	63	59
5	45	42	39
9	48	52	56

Table IV. Test Matrix (Runs) for Re = 2.15×10^6 Per Foot

CR	Run number at—		
	0 percent cowl	25 percent cowl	50 percent cowl
3	*66	62	*60
5	46	43	40
9	49	53, 54	57

*Indicates runs for which computed solutions are compared.

Pressure Measurements

Instrumentation response. The pitot pressures and mean surface static pressures were measured by an electronically scanned pressure (ESP) silicon sensor (ESP-32 model 780B, manufactured by Pressure Systems, Inc. (PSI)). The ESP modules each contain 32 sensors and were located inside a bay on the model to minimize tubing length and hence settling (lag) time. Pressures were observed to settle in less than 1 sec, allowing for very short run times and hence a minimum heating exposure to the model. In order to maintain the ESP modules at constant temperature, atmospheric air was bled into the ESP bay. Thermocouples placed in the bay on each module indicated that the temperature increased by no more than 1°F during the run. In anticipation of widely differing pressure ranges on the model, the pressure orifices were connected to modules rated for either 0.36, 2.5, or 5.0 psi full scale.

Calibration. The calibration of the ESP system was accomplished in situ prior to each run by sequentially applying three known pressures (chosen to span the range of expected measured pressures) to the ESP module and measuring the voltage output. From these three pressure-voltage points, a second-order curve fit defined the pressure-voltage relationship (which was essentially linear). The calibration coefficients for each pressure port were stored in the data acquisition computer (HP 9000-375 workstation) so that the output voltage could be converted to measured pressure. Calibration pressures (vacuum levels) were provided by connecting the modules to a turbomolecular vacuum pump and were measured by a DIGIQUARTZ calibration standard (a high-accuracy vibrating quartz pressure standard manufactured by Paroscientific, Inc.). The vacuum reference for the differential sensors was also provided by a turbomolecular vacuum pump.

Oil Flow Visualization

Surface flow visualization by means of surface oil flow has been common practice in many wind tunnel investigations. (See, for example, ref. 32 or 33.) The technique consists of applying a base coat of a low viscosity (in this case, 50 centistokes) vacuum oil to the surface of interest. For the present test, a nontoxic, nonirritating silicone fluid (available in a wide range of viscosities) was used. Discrete dots of a mixture of a higher viscosity (in this case, 200 centistokes) oil with white artist's paint were placed on the surface prior to the run. Postrun photographs of the oil streaks were used to obtain a qualitative indication of surface flow interactions.

Data Reduction and Uncertainty

Manufacturer specifications indicate that the overall pressure measurement system uncertainty was 0.07 percent of full scale. Thus the largest error was obtained when measuring the lowest pressures. For example, 0.07 percent of full scale for a 0.36 psi module corresponds to an uncertainty of 0.00025 psi. When measuring pressures in the vicinity of free-stream static (0.03 psi for Re = 2.15×10^6 per foot), this amounts to a relative uncertainty of 0.84 percent. At the lowest Reynolds number (0.55×10^6 per foot), the free-stream static pressure is approximately 0.009 psi, so at that level, the relative uncertainty would be 2.8 percent. For the 2.5 psi module, a 0.07 percent of full scale uncertainty corresponds to 0.00175 psi. Ideally this range would be used to measure pressures no lower than the maximum of the next lowest range pressure model (0.36 psi). In this case, the relative uncertainty is 0.5 percent. In order to prevent the 0.36 psi modules from being overscaled, orifices where the maximum anticipated pressure for any given configuration in the test matrix exceeded 0.3 psi were connected to the 2.5 psi module. This led to a few instances where for some configurations, the 2.5 psi module was used to measure pressures below 0.36 psi. For the Re = 2.15×10^6 per foot runs, the lowest measured pressure for this range module was 0.13 psi, and the corresponding relative uncertainty was 1.3 percent.

For the Re $= 0.55 \times 10^6$ per foot runs, the minimum pressure fell to approximately 0.07 psi, representing a relative uncertainty of 2.5 percent. The 5.0 psi modules were used strictly for pitot measurements, for which the worst case relative uncertainty was 0.35 percent. Thus for the high Reynolds number runs, the worst case relative uncertainty in the pressure measurements was 1.3 percent, and for the low Reynolds number runs, 2.8 percent. Run-to-run repeatability was examined for three configurations. Most gauges demonstrated repeatability to within 1 percent; however, for a few gauges the deviation reached as high as 4 percent, yielding an average run-to-run repeatability of within 2 percent. As discussed in reference 25, the uncertainty associated with the infrared surface temperature mappings was found to be less than 2 K over the 300 K to 375 K calibration range.

Computational Methods

The three-dimensional Navier-Stokes code SCRAMIN (ref. 19) was applied to the present study because it uses a well-known and well-proven numerical scheme and has shown favorable comparison with experiment at lower Mach numbers (2 to 6, which, as a result of this study, can be extended to 10). The code solves the three-dimensional Navier-Stokes equations in full conservation form by using MacCormack's time-asymptotic, explicit, predictor-corrector method (ref. 20). This method is second-order accurate in time and space and yields to a high degree of vectorization. The present work makes use of an algebraic grid-generation technique with linear connecting functions, described in reference 34, to obtain the Jacobian and metric data. In order to cluster the grid points near the boundaries in the physical domain, the grid refinement function of reference 35 is included in the transformation for the y and z coordinates.

Computational Grid

The computational surface grid for the configuration is presented in figure 9. It should be noted that the lateral scale has been exaggerated by a factor of 2 to offer a clearer depiction of the grid. The mesh has 86 grid points in the axial direction, 31 laterally, and 61 vertically (46 inside the inlet and 15 underneath—not shown—for the flow spillage). The grid is swept at the leading-edge sweep angle to better resolve interactions which occur in planes of constant leading-edge sweep. The sidewall leading edge is located at $i = 30$ and mounts to the forebody plane (baseplate) 9 in. aft of the baseplate leading edge. The throat begins at $i = 55$ (9.5 in. aft of the sidewall leading edge); the shoulder is also swept at the leading-edge sweep angle. The inlet exit (combustor entrance) is a vertical plane located at $i = 72$, 25 in. aft of the baseplate leading edge. As indicated in the figure, the inlet throat is longer near the baseplate than at the cowl plane because of the difference in sweep of the throat entrance and exit. In order to accommodate the swept throat entrance and vertical exit, the grid is linearly transitioned from swept to vertical in this region. The aft expansion added to the wind tunnel model to minimize tunnel blockage and to accommodate the rake mechanism was also modeled in the $i = 72$ to 86 region. The entire model was 30 in. long. After the desired grid was obtained, a final check on grid independence was performed by increasing the grid density by 50 percent in all three coordinates directions for the CR = 3, 0 percent cowl, Re $= 2.15 \times 10^6$ per foot configuration. Aside from a substantial increase in CPU time, no significant influence of the grid refinement on the engineering accuracy of the pressure distributions was noted. (Comparison of pressure distributions for both grids will be presented in the section "Comparison of Computation and Experiment.") The residual typically dropped 5 orders of magnitude in the convergence process.

Boundary and Initial Conditions

Because shock/boundary-layer interactions depend on the thickness and character of the incoming boundary layer, the inflow boundary was maintained at free-stream conditions and a laminar boundary layer was allowed to develop naturally on the 9 in. of flat plate upstream of the entrance plane of the inlet. An extrapolation boundary condition was applied at the exit plane. On solid surfaces, all velocity components as well as the normal pressure gradient are required to vanish. A constant temperature distribution (300 K) provided the thermal boundary condition. Open boundaries were calculated assuming vanishing normal gradients in velocity, temperature, and pressure. Because the flow field was symmetric, only half the field was computed and symmetry boundary conditions were imposed. The initial conditions were given by assigning free-stream conditions to each grid point except at the boundaries, where appropriate boundary conditions were applied.

Inflow Boundary Layer

Computationally, the leading edges were modeled as theoretically sharp, i.e., the effects of finite bluntness (0.010-in. radius) were neglected. For Re $= 2.15 \times 10^6$ per foot, the laminar-boundary-layer thickness (based on 99.5 percent of the edge velocity) at the inlet entrance station was found to be

0.35 in. The displacement thickness was computed to be 0.20 in., and the inlet inflow momentum thickness was 0.0076 in. The Reynolds number based on momentum thickness was $\mathrm{Re}_\theta = 1361.6$.

For $\mathrm{Re} = 0.55 \times 10^6$ per foot, the laminar boundary layer thickness was found to be 0.60 in. The displacement thickness was computed to be 0.32 in., and the inlet inflow momentum thickness was 0.0130 in. The Reynolds number based on momentum thickness was $\mathrm{Re}_\theta = 595.83$.

Tauber (ref. 36) presented empirical correlations of transition measurements. The equation $\mathrm{Re}_\theta / M_e = \text{Constant}$ was found to be an approximate correlation of the location of transition for boundary layers with supersonic or hypersonic edge velocities, where the constant varies between 150 and 350, depending upon the ratio of roughness height to momentum thickness among other parameters. For the Mach 10 inflow, the high and low Reynolds number test conditions yield values of $\mathrm{Re}_\theta / M_e = 136$ and 59.6, respectively, each of which is less than the value for transition.

Results and Discussion

During this test program, voluminous quantities of experimental data were obtained. Eight 32-channel pressure modules provided 256 channels of data (89 on the sidewall, 131 on the baseplate, with the balance reserved for the pitot rakes). For the wall static pressure measurements, the sampling rate was hardware limited to 4 frames/sec and a total of 40 frames (10 sec) of data. Each frame consisted of the average of eight samples. The data represent mean static pressure measurements. As previously noted, the pressures were observed to settle (asymptotically approach a constant value) in less than 1 sec, so data at 2 sec into the run are reported. (This time was selected to be late enough into the run to be assured of settled pressures and early enough to minimize heating to the model and hence the deviation from the constant temperature thermal wall boundary condition.)

In the interest of being concise, contour plots of the pressures on the baseplates and sidewalls are presented for comparison of the salient features among the configurations. Because the orifices were concentrated in the expected interaction regions, it was necessary to interpolate to obtain additional points to regularize the locations for the contour plotter, i.e., to create an $N \times M$ grid of pressure data. The pressure orifice locations are identified on the contour plots with a circle; the artificially generated (or phantom) points are indicated by the small crosshairs. Because the baseplate pressure orifices were arranged in lateral arrays, these data posed no difficulty to the contour plotter. For convenience, the outline of the cowl is drawn on the bottom of the sidewall contour figures to mark the cowl position. The contraction ratio is varied by positioning one sidewall progressively closer to the other; therefore, in the baseplate contour plots, the outline of the fixed sidewall is drawn. When the movable sidewall is positioned for CR = 9, a portion of that sidewall is visible in the plot and it is also sketched. At CR = 9, the movable sidewall covers nine pressure orifices (located on what was the centerline for CR = 3); therefore the resolution in the throat for that configuration is slightly diminished. In order to view the contours in the throat more easily, the y-scale is expanded by a factor of 3. In general, the contour plots show that the shock sheets generated by the swept leading edges glance across the baseplate, intersect at the centerline, and impinge on the sidewalls. If these interactions were purely inviscid, the sweep of the shock sheets would be preserved.

Individual line plots of the various static pressure distributions are also presented to provide a comparison of the relative magnitudes. Pressure orifices are located along a total of 53 lateral and axial arrays; data from a selected set of these arrays are plotted in reference 24. Only the axial pressure distributions on the baseplate, sidewall, and cowl centerlines, along with the lateral pressure distributions on the baseplate upstream of the sidewall/baseplate juncture, are presented here. In order to minimize the total number of line plots, these data are presented as comparison plots comparing the effects of contraction ratio, cowl position, or Reynolds number. First, the ratio of local to free-stream static pressure (p/p_∞) is presented along the centerline. Then the pressure distributions along 4 of the 25 lateral arrays on the baseplate (from the leading edge up to the inlet entrance plane) are presented. Following that, the pressure distributions on the centerline of the cowl and sidewall are presented. A general discussion of data trends and their relation to the internal flow physics is included. Computational contour plots and line plots for two configurations are presented to provide a direct comparison between experiment and computation.

Contraction Ratio Effects

Inviscid results. The effects of contraction ratio proved to be dominant, hence most of the discussion is directed at these effects. A simplified approximate analysis of the internal shock locations can be made by appropriately modifying two-dimensional oblique shock theory to accommodate the three-dimensional

effects of leading-edge sweep, i.e., spillage. (See ref. 37.) Shock locations determined in this fashion are used to graphically illustrate the internal shocks to orient the reader and are sketched for reference on the contour plots as dashed lines. (Note that this method approximates the shocks as planar sheets.) Table V provides the location of the inviscid glancing shock intersection at the centerline and the reflected shock sidewall impingements both in inches and as a percent of the distance from the leading edge to the throat ($x'/T_{x'}$) for CR = 3, 5, and 9. The table clearly demonstrates the forward progression of the shock interactions with increasing contraction ratio.

Table V. Inviscid Shock Impingement Locations

	Centerline		Sidewall impingement	
CR	x', in.	$x'/T_{x'}$	x', in.	$x'/T_{x'}$
3	8.02	0.84	10.08	1.06
5	6.68	.70	8.40	.88
9	6.01	.63	7.56	.79

Contour plot results. Figures 10(a) and (b) demonstrate the pressure contours on the inlet baseplate and sidewall for the CR = 3, Re = 2.15×10^6 per foot, 0 percent cowl configuration. The four primary interactions are evident in varying degrees. The baseplate pressure contours indicate that the leading-edge glancing shocks exert an upstream influence in the baseplate boundary layer near the centerline intersection. The baseplate boundary layer also tends to blur the centerline intersection. A localized expansion of the flow around the shoulder at the throat is observed on the baseplate by way of a low-pressure pocket just aft of the shoulder. The expansion is likewise evident on the sidewall plot (fig. 10(b)), as the axial pressure rise due to the shock impingement observed at the sidewall centerline does not extend to the baseplate. A region of lower pressure persists in the near corner region on the sidewall. As the computational results indicated (see ref. 25 for a full discussion), flow in the corner region follows the pattern referred to as an induced layer by Kubota and Stollery (ref. 38). The sidewall shock impingement is observed very near the shoulder. Computational baseplate and sidewall contours are presented in figures 10(c) and 10(d), respectively. It should be noted that some differences between the computed and the measured contours should be expected because of the effects of spacial resolution. (The computational grid on the sidewall surface provided pressures at 2021 points, compared with 89 static pressure orifices.) The forward extent of the upstream influence of the glancing shocks is slightly underpredicted, but both qualitatively and quantitatively, the flow interactions in the throat region are well captured. The cowl shock, formed as a result of the downturned flow impinging on the cowl, is observed to influence only a small percentage of the exit plane in both the computational and the experimental data.

Figures 11(a) and (b) form a similar set of plots for CR = 5 (0 percent cowl, Re = 2.15×10^6 per foot), and figures 12(a) and (b) correspond to CR = 9 (0 percent cowl, Re = 2.15×10^6 per foot). In the baseplate region, there are only two notable effects of contraction ratio in the experimental data: the expansion at the throat observed for CR = 3 is not seen for the higher contraction ratios (in part because of the effective decrease in experimental lateral resolution with increasing contraction ratio and the overall higher pressures dominating the region due to the more forward shock impingements), and a quantitative increase in the overall static pressure with increasing contraction ratio. This increase is believed to be the result of a small separation region which forms ahead of the glancing shock. Computationally (ref. 25) it was demonstrated that there is turning in the baseplate boundary layer significantly ahead of the inviscid shock location, i.e., strong induced cross flows are observed well ahead of the glancing shock location. Figure 13 shows the cross-flow velocity vectors at $x'/T_{x'} = 0.40$ for the CR = 3, Re = 2.15×10^6 per foot, 0 percent cowl configuration. The shock is observed to be at 45 percent of the semispan of the inlet, while the induced cross flow has already reached the centerline. An increase in the contraction ratio would effectively move the centerline closer to the sidewall. This means that a stronger cross flow impinges on the centerline (i.e., larger cross-flow separation region) and that the centerline impingement of the cross flow occurs at a more forward location. The resultant separation therefore increases in size with increasing contraction ratio. (The size and extent of the forward separation is discussed in the section "Surface Streamlines.")

By far the most dramatic contraction ratio effects are observed on the inlet sidewall. The shock is observed to impinge at approximately the shoulder for CR = 3, but for CR = 5 the impingement has moved to approximately $x'/T_{x'} = 0.78$ (somewhat ahead of the inviscid impingement point of 0.88). For CR = 9, the impingement occurs at $x'/T_{x'} = 0.68$ (compared with the inviscid location of 0.79). The impingement ahead of the inviscid location should be no surprise, because the displacement of the sidewall boundary

layer has the effect of increasing the wedge angle and hence the shock strength, causing the shock to strike both the centerline and the sidewall at more forward positions. For CR = 5, the pressure is observed to rise following the shock impingement (fig. 11(b)) until the shoulder is reached. A localized expansion is noted on the sidewall in the centerline region prior to the recompression of the second impingement at approximately $x'/T_{x'} = 1.2$. The shocks and expansion are observed to be attenuated toward the baseplate as a result of the corner flow and the baseplate boundary-layer separation, the disturbance appearing to emanate from the juncture of the leading edge of the sidewall and the baseplate.

The cowl shock also appears to become more prominent for increasing contraction ratio. Because the shock impingements occur farther forward for increasing contraction ratio, the flow in the throat region has passed through more shocks, each of which has enhanced the downturning of the flow, as the contraction ratio is increased. Hence the cowl shock becomes stronger, since the flow incidence angle is greater for increased contraction ratio. The plot for CR = 5 shows a cowl shock which is stronger and extends farther up into the exit plane. Even though the cowl has not been moved, the postcowl shock region becomes a larger percentage of the exit plane, enhancing any vertical asymmetry in the exit plane.

Similar features become even more strongly accentuated at CR = 9. At the throat, the sidewall static pressures down to $Z/H = 0.5$ have been perturbed by the corner flow and the baseplate boundary-layer separation. Additionally, the cowl has also increased its domain of influence on the sidewall, as previously discussed. The first sidewall impingement is located at $x'/T_{x'} = 0.68$, with a second impingement at approximately 1.03. Significantly higher pressures in the cowl region are noted, since the flow near the cowl has passed through three shocks, each of which have incrementally increased the downturning. The postcowl shock region is seen to affect approximately 25 percent of the exit plane.

Line plot results. A more rapid assessment of the relative magnitudes of the static pressure distributions is afforded by the line plots. Figure 14 presents the contraction ratio effects for the Re = 2.15×10^6 per foot, 0 percent cowl configuration. Figure 14(a) shows the pressure distributions for CR = 3, 5, and 9 along their respective centerlines. The hypersonic viscous interaction is evident in that the pressure is observed to be higher near the leading edge ($p/p_\infty \approx 2.3$ at 1 in. aft of the leading edge, $x'/T_{x'} = -0.841$), relaxing back to $p/p_\infty \approx 1.7$ near the inlet entrance. For CR = 3, the pressure is observed to rise slightly near the inlet entrance ($x'/T_{x'} = 0.11$) to a plateau of $p/p_\infty \approx 2.3$. The pressure remains relatively constant at that level until it gradually ramps up (beginning at $x'/T_{x'} = 0.6$) to $p/p_\infty = 8.5$ at the inlet throat. The effects of the corner expansion are observed, as the pressure relaxes slightly over the next three orifices to $p/p_\infty = 8.0$. A secondary rise to $p/p_\infty = 8.2$ is noted at $x'/T_{x'} = 1.3$. At this point, the compression then drops to approximately 7.5 and begins a gradual rise toward the exit. This sawtooth pattern is the result of a multiply reflecting internal shock. The computational results of reference 25 suggest that the pressures observed on the baseplate do not well indicate the compression of the core flow of the inlet because of the vortical interactions resulting from the induced cross flow on the baseplate; but it is noted here that the effects of the glancing shocks, although perhaps tempered by the vortical flow, nevertheless influence the baseplate static pressures. The inviscid shock calculations indicate that the leading-edge shock should reach the centerline at $x'/T_{x'} = 0.84$ (table V). The location of the initial pressure rise in the data indicates significant upstream influence of the crossing shock pattern. It is interesting that for CR = 5 and 9, a higher pressure is noted ahead of the inlet entrance plane than for CR = 3. At $x'/T_{x'} = -0.1$, a compression of 2.5 is noted, compared with approximately 1.7 for CR = 3.

Of the three effective centerlines, the centerline corresponding to the CR = 3 is the most densely populated with pressure orifices. In figure 14(b), this array is used to indicate the forward extent of the upstream pressure rise for CR = 5 and 9 (see fig. 14(a), despite the fact that this array of orifices is slightly off centerline for these configurations. The figure shows that the first indication of a pressure rise on the baseplate for the higher contraction ratios occurs at $x'/T_{x'} = -0.38$.) This may be indicative of a separation caused by the crossing shocks which has fed forward of the inlet entrance. For CR = 5 and 9, the pressure is observed to gradually increase toward the throat, in contrast to the plateau region noted for CR = 3. For CR = 5, the pressure rise becomes more significant at $x'/T_{x'} = 0.63$, reaching a peak compression of $p/p_\infty = 11.0$ at the throat. The location of the sudden increase in compression is noted to be near the intersection of the inviscid shock and the centerline ($x'/T_{x'} = 0.70$), again indicating significant upstream influence, not only in that the pressure rise begins ahead of the intersection of the inviscid shock and the centerline, but also in that the pressure increase is observed to cause a

gradual increase in pressure from as far forward as the inlet entrance, rather than from a plateau as at CR = 3. Aft of the shoulder, the pressure expands to a compression of 10.5 before rapidly rising to 11.5 at $x'/T_{x'} = 1.24$. A gradual decrease in compression is again noted until a local minimum of 11.0 is reached at $x'/T_{x'} = 1.41$. An increase in compression is then noted to a maximum of 13 at the inlet exit. Again the sawtooth pattern, which in this instance rises and falls with greater frequency than for the CR = 3 configuration because of the forward movement of impingement points (and hence more impingements within the same length) with increased contraction ratio, indicates that the viscous, vortical baseplate flow has not entirely isolated the baseplate from the pressure rise associated with the glancing shocks. The pressure rise for CR = 9 is observed to be much greater than for CR = 3 or 5. Beginning at $x'/T_{x'} = 0.60$, the pressure is observed to rise rapidly to the throat entrance. While this location appears to correspond well with the inviscid prediction of the shock intersection at the centerline ($x'/T_{x'} = 0.63$), the upstream influence of the crossing shocks is noted via the gradual increase in compression from the entrance plane of the inlet. The pressure rise in the inlet is observed to be rapid, interrupted by the expansion at the shoulder of the throat. The expansion does not cause the pressure to relax, but rather tempers the strong pressure rise, keeping the compression at approximately 23.5 between $x'/T_{x'} = 1.0$ and 1.07. A peak compression of 37 is noted at $x'/T_{x'} = 1.58$ ($x'/T_{x'} = 1.68$ shows a significant drop in pressure as the flow begins to expand out the aft end of the inlet). The previously noted sawtooth pattern is no longer observed.

Figures 14(c)–(f) present the lateral pressure distributions across the baseplate at axial stations beginning 1 in. from the baseplate leading edge and proceeding downstream to the inlet entrance plane. It should be noted that the same pressure orifices were used for each contraction ratio, but because the effective centerline moves as a result of achieving increased contraction ratio by moving only one sidewall, the orifices have different lateral positions relative to the centerline ($x'/T_{x'}$) for different contraction ratios. At 1 in. aft of the baseplate leading edge ($x'/T_{x'} = -0.8412$), the pressures are observed to be uniform for each of the contraction ratios at $p/p_\infty = 2.2$ (fig. 14(c)). At $x'/T_{x'} = -0.5258$ (fig. 14(d)) however, the pressure distributions for CR = 5 and 9 begin to deviate from the distribution for CR = 3. The apparent separation region which influenced the axial data is here observed to have a significant upstream extent. The overall pressure level has decreased, however, from the upstream station. The highest compression at this station for any of the contraction ratios was 1.7. At $x'/T_{x'} = -0.1052$ (fig. 14(e)), the increased pressures for the higher contraction ratios are clearly noted, as the compression for CR = 5 and 9 is approximately 2.4, compared with 1.35 for CR = 3. Also of interest is the uniformity of the lateral pressure distribution for CR = 3, in contrast with the dome-shaped pressure distribution for the higher contraction ratios. A pressure relief is noted outboard of the location of the two inlet sidewalls. At the inlet entrance station ($x'/T_{x'} = 0$), figure 14(f) shows that the CR = 3 distribution indicates a slight increase in pressure near the inlet sidewall leading edge. The data show that the compression for CR = 5 and 9 is nearly twice that for the CR = 3. A pressure relief is noted near the sidewall leading edge as some of the high-pressure, separated flow spills around the side of the inlet. This situation would be different for a flight vehicle with multiple engine modules. A lower pressure region outboard of the inlet sidewall (toward which the flow could turn) would not be available because of the presence of additional engine modules. This outboard turning will be clearly demonstrated in the oil flow photographs.

Figure 14(g) shows the pressure distribution on the cowl centerline for each contraction ratio. As has been previously indicated, the flow downturning and local static pressure are increased incrementally by each reflected shock through which the flow passes. Thus, the higher contraction ratio cases have higher cowl pressures, because the cowl shock is stronger for higher contraction ratios. This trend is reflected in the data. The CR = 3 cowl pressure distribution shows little effect of the crossing shock pattern. (It should be noted that the exit plane on the cowl surface is $x'/T_{x'} = 1.26$, and data beyond that point are subject to the expansion of the sidewalls aft of the exit plane.) The average compression over the first half of the cowl length for the CR = 5 data is 55, nearly twice the value for the CR = 3 data. In addition to the increased downturning, the increased number of reflected shocks has also increased the static pressure, which combined with a stronger cowl shock yields a large increase in compression on the cowl. The same is also true (and to an even greater extent) for the CR = 9 data. An average value for the CR = 9 cowl surface compression is approximately 170, in excess of three times the compression for the CR = 5 data.

Pressure distributions down the centerline of the fixed sidewall are found in figure 14(h). The forward progression of the shock impingement is well

indicated. The pressure rise for the CR = 3 data does not occur until $x'/T_{x'} = 1.07$; whereas for the CR = 5 data, the first pressure peak occurs at approximately $x'/T_{x'} = 0.90$. The expansion aft of the impingement brings the pressure to a minimum compression of 11 at $x'/T_{x'} = 1.07$. The second sidewall shock impingement is observed to increase the compression to another local maximum of 24. Following the peak is another trough of approximately 11 at $x'/T_{x'} = 1.32$. At the exit plane, the pressure is again rising. The sawtooth pattern clearly indicates multiple shock impingements, and their locations correspond well with the predicted values. The CR = 9 data indicate a peak compression of approximately 30 at $x'/T_{x'} = 0.84$. There is a slight relaxation of pressure prior to the throat, but no local expansion at the throat is observed. The next compression peak ($p/p_\infty \approx 64$) occurs aft of the shoulder at $x'/T_{x'} = 1.15$.

Surface streamlines. Surface streamlines obtained using the oil flow technique also provide an insight into the contraction ratio effects as well as the internal flow structure. Figures 15(a)–(f) are postrun photographs of the oil streaks for three different configurations. Figure 15(a) shows the interior wall of the inlet (one sidewall and the cowl were removed following the run for the photographs) for the CR = 3, Re = 2.15×10^6 per foot, 0 percent cowl configuration. Several features are evident. The compression from the boundary-layer growth at the baseplate leading edge is evident in the lower half of the inlet. A weak feathered pattern is noted just below a line of convergence on the sidewall near the baseplate/sidewall juncture, possibly indicating the presence of a secondary corner vortex. The line of convergence and the stagnant region in the immediate corner are consistent with the induced layer previously discussed. Additionally, because the sidewall shock impinges very near the shoulder, no large-scale separation regions are noted on the sidewalls in the vicinity of the impingement. A single line of convergence is noted arcing from the baseplate just upstream of the shoulder and may be the only indication of a separation. Multiple axial lines of convergence (possibly the result of vortices shed from the shock impingement) are noted in the throat downstream of the impingement.

Figure 15(b) demonstrates the forward progression of the shock impingement (for CR = 5) and the strong downturning/separation associated with the impingement. This photograph more clearly shows the vortex located just below the line of convergence on the sidewall. Additionally, the effects of the baseplate leading-edge compression are also evident at about the half-height of the inlet sidewall. Near the cowl plane, the oil streaks indicate strong downturning at the first impingement point. A second swept line of convergence is noted in the throat at the second sidewall impingement point.

At CR = 9, figures 15(c)–(f) indicate that the dominant flow feature is the large-scale separation on the baseplate. Near the baseplate leading edge, the oil streaks are observed to flow uniformly downstream until approximately $x'/T_{x'} = -0.4$. (This corresponds well to the observed pressure rise on the baseplate at $x'/T_{x'} = -0.38$, fig. 14(b).) In the immediate vicinity of the sidewall leading edge, the surface streamlines indicate that the flow on the surface is moving upstream and is spilling around the outside of the inlet, as was suggested by the dome-shaped spanwise pressure distribution for CR = 5 and CR = 9 at $x'/T_{x'} = -0.1$, figure 14(e). As was previously noted, this flow pattern would not be duplicated exactly on a multiengine flight vehicle because there would be no lateral pressure relief due to the presence of other identical engine modules on either side of a given module. Because of this lack of a lateral pressure relief, this separation would likely be more severe on a multiengine model.

The presence of such a large-scale separation leads to the question of whether the inlet has indeed started. In the classical sense, an unstarted inlet would be characterized by a normal shock stationed upstream of the entrance, with greatly enhanced spillage and minimal mass capture, total pressure recovery, etc. The presence of oblique shock impingements on the sidewalls coupled with measured static pressures well below postnormal shock values contradicts a classical unstart. However, the presence and extent of such large regions of reversed flow undoubtedly adversely affects the performance and efficiency of the inlet. Data are presented in reference 24 for the CR = 9, 50 percent cowl configuration at Re = 1.14×10^6 per foot that show a change in the character of the flow, suggesting that the combination of high contraction ratio, low Reynolds number, and forward cowl may promote a classical unstart.

Cowl Position Effects

Contour plot results. Cowl position effects can be examined by comparing the data for 0 percent cowl and 50 percent cowl at CR = 3, Re = 2.15×10^6 per foot. The 50 percent cowl configuration is presented in figure 16. Comparison of the experimental data in figures 10(a) and 16(a) and the computational data in figures 10(c) and 16(c) indicates that the cowl position has little effect on the baseplate.

Sidewall experimental (figs. 10(b) and 16(b)) and computational (figs. 10(d) and 16(d)) contour plots show an influence in the vicinity of the cowl. For CR = 3, the (inviscid) glancing shock reaches the centerline at $x'/T_{x'} = 0.84$, returning to the sidewall at $x'/T_{x'} = 1.06$. Thus, over half the region between the glancing shock from the sidewall leading edge and its centerline reflection is enclosed by the cowl. In this instance, much of the flow which would have spilled out for the 0 percent cowl configuration has been captured by the cowl. Because this flow has been turned downward by only the initial glancing shock, the cowl shock is weak and deflects some of the pressure contours from the impingement region forward. A region of significantly higher pressure develops at the impingement of the shock on the sidewall. As this shock reflects back toward the centerline, the flow downturning is increased, yielding a region of flow impinging on the cowl and correspondingly higher pressures.

Line plot results. Figure 17 presents the cowl position effects on the baseplate, sidewall, and cowl pressure distributions. Examination of the centerline pressure distribution for CR = 3, Re = 2.15×10^6 per foot configuration (fig. 17(a)) indicates that forward cowl placement produces no change in the character of the incoming flow field (as was observed for increasing contraction ratio), i.e., the pressure distributions remain laterally uniform. Figures 17(b)–(f), however, illustrate the worst case average repeatability/uncertainty of approximately 4 percent.

The cowl pressures are shown in figure 17(g). The pressures for the three cowl positions appear to overlap each other, indicating that the pressure distribution on the cowl is driven primarily by the internal shock locations as well as the location of the orifice relative to the throat entrance. It was demonstrated computationally (ref. 25) that a major constituent of the sidewall/baseplate corner flow is induced cross flow. A similar induced cross flow is initiated at the cowl, and because of the proximity of the sidewalls at the throat, the cross flow rapidly reaches the centerline, forming recirculation regions which dominate the span. This cross flow is enhanced by the downturning imparted to both the core flow and the sidewall flow by the glancing shocks.

The axial pressure distribution on the sidewall centerline (fig. 17(h)) indicates that the effects of the cowl are very small relative to the magnitude of the pressure. Holland (ref. 24) presents complete data sets for cowl placement comparison for the CR = 3, Re = 1.14×10^6 per foot and Re = 0.55×10^6 per foot configurations in addition to the Re = 2.15×10^6 per foot configuration (this set also includes CR = 5 and 9 for all three Reynolds numbers).

Reynolds Number Effects

Contour plot results. Reynolds number effects can be identified by comparison of data from the CR = 3, 0 percent cowl configuration at Reynolds numbers per foot of 2.15×10^6 (discussed in the preceding sections) and 0.55×10^6. Figures 18(a) and (b) are comparable to the plots already presented for Re = 2.15×10^6 per foot (figs. 10(a) and (b)). Decreasing the Reynolds number indicates by definition that the viscous forces take on greater significance with respect to the momentum forces. Hence, boundary-layer thicknesses are expected to increase and, more importantly to the inviscid flow field, the displacement thicknesses increase, causing all surfaces to possess effectively larger wedge angles. This in turn causes the sidewalls to generate slightly stronger shocks and increases the internal compression of the inlet. Beyond the displacement effects, an increased boundary-layer thickness influences the shock impingements and reflections and may increase the degree of flow separation. Because the range of Reynolds numbers obtainable in the present facility spans less than an order of magnitude, large changes in the flow structure were not anticipated; however, it will be demonstrated in the line plots that large changes in the flow structure did indeed occur over this small range of Reynolds number.

For both Reynolds numbers presented, the baseplate pressure contours demonstrate the nominal interactions previously discussed. Pressure levels in general tend to decrease with increasing Reynolds number. For example, a comparison of the location of the $p/p_\infty = 4.0$ contour in figures 18(a) and 10(a) (CR = 3, 0 percent cowl) indicates that the pressure rises to this level by $x'/T_{x'} = 0.85$ for Re = 2.15×10^6 per foot and by $x'/T_{x'} = 0.55$ for Re = 0.55×10^6 per foot. The forward movement of the pressure rise is indicative of an increasing glancing shock strength due to increased sidewall boundary-layer thickness with decreasing Reynolds number as well as to the increased viscous interaction of the shock with the baseplate boundary layer (upstream influence) and the enhanced viscous corner flow. This is observed for all the contraction ratios and cowl positions (ref. 24). The fact that the interaction is observed to be more distinct for the lower Reynolds numbers is in part due to the increased physical size of the lower Reynolds number interaction regions. These interactions, which span several static pressure orifices, are more easily resolved

experimentally. Although a total of 89 static pressure orifices are located on the sidewall, there still exists significant spacing between the orifices. The average instrumentation density on the sidewall is given by 89 orifices/56 in^2 = 1.6 orifices/in^2, although the orifices were clustered to improve the density in interaction regions. Interpolating among data points to locate lines of constant pressure adds an additional smearing effect. Thus, larger scale interactions (those which influence multiple orifices) are better displayed in the contour plots. Particularly for CR = 3, the lower Reynolds number contours appear to be better defined.

Line plot results. A more quantitative comparison of the Reynolds number effects on the static pressure distribution is provided by the line plots. The Reynolds number effects for the CR = 3, 0 percent cowl configuration are demonstrated in figure 19. It is clear from figure 19(a) that the Reynolds number has a significant impact on the flow structure (and hence pressure distribution). The viscous interaction is observed at the leading edge of the baseplate; additionally, the compression on the baseplate is observed to increase because of the increased boundary-layer growth with decreased Reynolds number. The pressure rise on the baseplate due to the glancing shock interaction is observed to move forward with decreasing Reynolds number, and is located at $x'/T_{x'} = 0.1$ for Re = 2.15×10^6 per foot and at $x'/T_{x'} \approx -0.2$ for the lower Reynolds numbers (forward of the inlet entrance). The glancing shock impingement on the sidewall (aft of the shoulder at Re = 2.15×10^6 per foot) is anticipated to move forward with decreased Reynolds number as a result of increased sidewall displacement thickness. The throat pressure distribution becomes much more uniform when the shock impingement moves forward toward the shoulder; the sharp increase in pressure due to the shock is tempered by the throat expansion. (For an inviscid reflection, the shock would be said to cancel if impingement occurred at the shoulder.) The increased flat plate compression is also observed in the lateral pressure distributions (figs. 19(b)–(e)). The flow separation ahead of the inlet is observed in figure 19(d) at $x'/T_{x'} = -0.1052$. At the high Reynolds number, the pressure distribution is uniform; however, at Re = 1.14 and 0.55×10^6 per foot, the pressure is not only higher than at $x'/T_{x'} = -0.52$ (the next upstream station), but it demonstrates a significant pressure relief as the flow spills around the outside of the inlet sidewalls. (The outboard flow spillage for the lower Reynolds number is quite similar to that seen with increased contraction ratio, as observed in the comparison of figs. 19(d) and 14(e).) Even at the low contraction ratio, a decrease in Reynolds number of less than an order of magnitude can trigger significant forward separation. (Ref. 24 shows that this forward separation grows with decreased Reynolds number for all contraction ratios tested.) The cowl pressures (fig. 19(f)) also appear particularly sensitive to Reynolds number.

The axial sidewall centerline pressure distribution is given in figure 19(g). Again, an overall increase in compression is noted, primarily by way of increased compressive turning due to the increased displacement thickness with decreased Reynolds number. The forward progression of the sidewall shock impingement is particularly evident. At Re = 2.15×10^6 per foot, the pressures climb to a plateau at $x'/T_{x'} = 1.2$. The peak moves forward to approximately $x'/T_{x'} = 1.06$ for Re = 1.14×10^6 per foot. At Re = 0.55×10^6 per foot, the peak pressure is noted at approximately $x'/T_{x'} = 0.96$. A factor of 4 decrease in Reynolds number has demonstrated a significant movement of the internal shock structure, moving the sidewall shock impingement from aft of the throat to upstream of the throat. Although the Reynolds number has not been changed enough to change the character of the inflow boundary layer, the entire character of the interaction may be altered, i.e., large-scale forward separation has been promoted because of the relatively small decrease in Reynolds number. Only the CR = 3, Re = 2.15×10^6 per foot configuration performed "on design," i.e., without large forward separations. Caution must therefore be exercised in wind tunnel and computational simulations as to the Reynolds number and Mach number matching of a proposed flight condition.

Comparison of Computation and Experiment

Line plot results. In order to assess how well the results from both phases compliment each other, an explicit comparison of the computational and experimental results is necessary. Results are presented for the CR = 3, Re = 2.15×10^6 per foot configuration with both 0 percent and 50 percent cowl. Figure 20 shows good quantitative agreement for the 0 percent cowl. The pressure peak at the throat on the baseplate is overpredicted by about 10 percent, but the sidewall pressure distribution shows an extremely close fit. Figure 21 corresponds to the 50 percent cowl configuration. Again good quantitative agreement is achieved on the baseplate and sidewall centerlines.

A grid independence study was performed for this configuration by increasing the grid density by 50 percent in all three coordinate directions, with no appreciable change in the solution noted. (Fig. 20 presents the baseplate and sidewall centerline pressure distributions for both grid configurations.) The CR = 3 configuration was selected for the study because it represented the widest throat gap, and hence poorest lateral resolution, if the number of grid points in each coordinate direction were selected to be common among the grids for each contraction ratio. Thus, if a resolved grid could be identified for the CR = 3, it was felt that a similar grid for the higher contraction ratios would possess effectively better resolution in the throat and thus the expense of individual grid independence studies could be spared. The solutions were run prior to the experiment, i.e., without a priori knowledge of the experimental flow interactions. The experiment uncovered a fundamental change in the flow structure with either increasing contraction ratio or decreasing Reynolds number by way of large-scale separations. Because of this change in the character of the flow (and hence change in the pertinent length scale), the grid independence study for the CR = 3 configuration was deemed insufficient to show grid independence for the other configurations. Further, the assumption of laminar flow on all surfaces may no longer be valid in the more strongly interacting flow fields. Thus, computational data for the higher contraction ratio configurations are not shown.

Exit plane rake comparisons. A movable rake containing 11 pitot probes was installed inside the inlet to survey the exit plane. (See fig. 3.) The 11 probes were manufactured of stainless steel tubing with a 0.0625-in. outside diameter and a 0.040-in. inside diameter. The tubes were spaced 0.285 in. apart and positioned in the inlet to vertically span the center 2.85 in. Prior to the run, the rake was positioned flush against the inlet sidewall. During the run, the rake was moved to and paused at nine lateral locations between the sidewall and the inlet centerline by a microprocessor-based stepper motor controller. Prior to completion of the run, the rake was returned to its initial position to demonstrate repeatability with the initial pressure measurement. (Initial tests were performed with the rake traversing the entire throat width to determine lateral symmetry. Thereafter, the measurements were concentrated across the half-width.)

Figure 22 presents pitot rake data taken in the exit plane of the inlet compared with the computed values for the CR = 3, 0 percent cowl configuration at Re = 2.15×10^6 per foot. The data principally show the exit plane shock structure and the good qualitative and quantitative agreement between the experimental and the computational data. Near the sidewall, the shape of the experimental contours indicates some interference effects from the sidewall. This is an expected result, because pitot measurements are highly intrusive. Based on schlieren photographs of a 1/16-in-diameter pitot probe in a Mach 6 free stream (the approximate throat Mach number), the bow shock formed around the probe has a standoff distance of one-fourth of the probe diameter and, at the throat face, the diameter of the shock is 1.5 probe diameters. The interaction between the probe bow shock and the sidewall boundary layer increases the region influenced by the probe. Mechanical difficulties related to stepper motor failure prevented accurate experimental pitot measurements for the CR = 3, Re = 2.15×10^6 per foot, 50 percent cowl configuration, i.e., the rake mechanism stalled near the wall. Nevertheless, computational pitot contours are presented for comparison (fig. 23). Comparison of these data with the computational data from the 0 percent cowl data (fig. 22) indicates that the only significant effect of cowl position on pitot pressure is in terms of the corner vortex generated by the sidewall/cowl juncture. The vortical interaction is significantly larger for the 50 percent cowl because the forward cowl placement allows more time (and length) over which to evolve. Overall, the flow field measurements and the computed pitot pressures compare quite favorably. This lends credence to the remainder of the computed exit plane properties.

Concluding Remarks

A combined computational and experimental parametric study of the internal aerodynamics of a generic three-dimensional sidewall compression scramjet inlet configuration has been performed (1) to demonstrate the utility of computational fluid dynamics (CFD) as a design tool in hypersonic inlet flow fields, (2) to examine the nature and structure of the flow interactions inside an inlet subject to a high Mach number laminar inflow, and (3) to provide a comprehensive surface property and flow field database to determine the effects of contraction ratio (CR), cowl position, and Reynolds number (Re) on the performance of a hypersonic scramjet inlet configuration. Computational fluid dynamics is used to drive the design of the experimental configuration; the experimental work is in turn used to provide a validation for the computational parametrics. A summary of the observations made in the study are presented as follows.

Shocks formed on the sidewall leading edges are observed to glance across the baseplate, intersect at the centerline, and impinge on the sidewalls. The induced corner flow and upstream influence of the glancing shocks are observed to be significant. With increasing contraction ratio, the separation generated by the glancing shocks is observed to grow and, for CR = 5 and 9, extend forward of the inlet entrance. A decrease in the free-stream unit Reynolds number by only a factor of two led to a similar upstream separation. On a multiengine model (or flight vehicle) the magnitude of such separation is anticipated to be larger because of the lack of lateral pressure relief resulting from the presence of neighboring identical engine modules. Although the presence of such large-scale separations leads to the question of whether the inlet is started, the presence of internal oblique swept shock interactions on the sidewalls seems to indicate that, at least in the classical sense, the inlet is not unstarted. However, the combination of high contraction ratio, low Reynolds number, and forward cowl appeared to promote a classical unstart. Undoubtedly, the presence and extent of these large upstream separation regions adversely affect the performance and efficiency of the inlet. The laminar inflow boundary layer therefore appears to be very sensitive to increases in contraction ratio or decreases in Reynolds number; of the configurations tested, only the CR = 3 configuration with 0 through 50 percent cowl at Re = 2.15×10^6 per foot operated "on design."

Multiply reflecting internal swept shocks were observed to incrementally increase the downturning (as well as the pressure) of the flow. The overall compression of the inlet was therefore observed to increase with increasing contraction ratio, as was the strength of the cowl shock. Further, a forward placement of the cowl was observed to increase the mass capture by preventing the flow downturned by these internal shocks from spilling out of the inlet.

Good quantitative agreement was obtained between computation and experiment for the CR = 3 configuration at Re = 2.15×10^6 per foot for both 0 and 50 percent cowl positions. The fundamental change in flow interactions with decreased Reynolds number or increased contraction ratio rendered the grid independence study performed for CR = 3 inconclusive for application to other configurations. Hence, computational results for other configurations are not presented. This highlights the need for the coupling of CFD with experiment. While CFD provided detailed information about the flow field, experiment uncovered the fundamental changes in the flow field which required a change in the computational modeling.

NASA Langley Research Center
Hampton, VA 23681-0001
October 18, 1994

References

1. Barthelemy, Robert R.: Face to Face. *Aerosp. America*, vol. 29, no. 9, 1991, pp. 6–9.
2. Williams, Robert M.: National Aero-Space Plane: Technology for America's Future. *Aerosp. America*, vol. 24, no. 11, 1986, pp. 18–22.
3. Kandebo, Stanley W.: Researchers Pursue X-30 Spaceplane Technologies for 1990 Evaluation. *Aviat. Week & Space Technol.*, vol. 129, no. 6, 1988, pp. 49, 53.
4. Kandebo, Stanley W.: NASP Cancelled, Program Redirected. *Aviat. Week & Space Technol.*, vol. 138, no. 24, 1993, pp. 32, 34.
5. Henry, John R.; and Anderson, Griffin Y.: *Design Considerations for the Airframe Integrated Scramjet.* NASA TM X-2895, 1973.
6. Trexler, Carl A.: Performance of an Inlet for an Integrated Scramjet Concept. *J. Aircr.*, vol. 11, no. 9, 1974, pp. 589–591.
7. Trexler, Carl A.: Inlet Performance of the Integrated Langley Scramjet Module (Mach 2.3 to 7.6). AIAA-75-1212, 1975.
8. Trexler, Carl A.; and Souders, Sue W.: *Design and Performance at a Local Mach Number of 6 of an Inlet for an Integrated Scramjet Concept.* NASA TN D-7944, 1975.
9. Holland, Scott D.; and Perkins, John N.: Mach 6 Testing of Two Generic Three-Dimensional Sidewall Compression Scramjet Inlets in Tetrafluoromethane. AIAA-90-0530, 1990.
10. Holland, Scott D.; and Murphy, Kelly J.: An Experimental Parametric Study of Geometric, Reynolds Number, and Ratio of Specific Heats Effects in Three-Dimensional Sidewall Compression Scramjet Inlets at Mach 6. AIAA-93-0740, 1993.
11. Vinogradov, V. A.; Stepanov, V. A.; and Alexandrovich, E. V.: Numerical and Experimental Investigation of Airframe-Integrated Inlet for High Velocities. AIAA-89-2679, 1989.
12. Kanda, T.; Komuro, T.; Masuya, G.; Kudo, K.; Murakami, A.; Tani, D.; Wakamatsu, Y.; and Chinzei, N.: Mach 4 Testing of Scramjet Inlet Model. AIAA-89-2680, 1989.
13. Settles, Gary S.; and Dolling, David S.: Swept Shock Wave/Boundary-Layer Interactions. *Tactical Missile Aerodynamics*, Volume 104, AIAA, 1986, pp. 297–379.
14. Settles, G. S.; and Dolling, D. S.: Swept Shock/Boundary-Layer Interactions—Tutorial and Update. AIAA-90-0375, 1990.

15. Knight, Doyle D.; Horstman, C. C.; and Settles, Gary S.: Three-Dimensional Shock Wave-Turbulent Boundary Layer Interactions Generated by a Sharp Fin at Mach 4. AIAA-91-0648, 1991.

16. Reddy, D. R.: *The 3-D Navier-Stokes Analysis of Crossing, Glancing Shocks/Turbulent Boundary Layer Interactions.* NASA TM-104469, 1991.

17. Narayanswami, Natraj: A Numerical Investigation of the Interaction Between Crossing Oblique Shocks and a Turbulent Boundary Layer. Ph.D. Diss., Rutgers Univ., 1992.

18. White, M. E.; Drummond, J. P.; and Kumar, A.: Evolution and Application of CFD Techniques for Scramjet Engine Analysis. *J. Propuls. & Power*, vol. 3, no. 5, 1987, pp. 423–439.

19. Kumar, Ajay: *Numerical Simulation of Scramjet Inlet Flow Fields*. NASA TP-2517, 1986.

20. MacCormack, Robert W.: The Effect of Viscosity in Hypervelocity Impact Cratering. AIAA-69-354, 1969.

21. Kumar, Ajay: Numerical Analysis of a Scramjet Inlet Flow Field Using the Three-Dimensional Navier-Stokes Equations. *Computational Methods for Ramjets*, Debra Sue Eggleston, ed., CPIA Publ. 373 (Contract N00024-83-C-5301), Appl. Phys. Lab., Johns Hopkins Univ., 1983, pp. 25–39.

22. Holland, Scott D.: *Computational Parametric Study of Sidewall-Compression Scramjet Inlet Performance at Mach 10.* NASA TM-4411, 1993.

23. Holland, Scott D.; Hodge, Jeffrey S.; and Perkins, John N.: Wind Tunnel Blockage Study of a Generic Three-Dimensional Sidewall Compression Scramjet Inlet at Mach 10. AIAA-91-0294, 1991.

24. Holland, Scott D.: *Mach 10 Experimental Database of a Three-Dimensional Scramjet Inlet Flow Field.* NASA TM-4648, 1995.

25. Holland, Scott D.: *Mach 10 Computational Study of a Three-Dimensional Scramjet Inlet Flow Field.* NASA TM-4602, 1995.

26. Holland, Scott D.: A Computational and Experimental Investigation of a Three-Dimensional Hypersonic Scramjet Inlet Flow Field. Ph.D. Diss., North Carolina State Univ., 1991.

27. Peñaranda, Frank E.; and Freda, M. Shannon: *Aeronautical Facilities Catalogue.* Volume 1—Wind Tunnels. NASA RP-1132, 1985.

28. Miller, C. G.: Langley Hypersonic Aerodynamic/Aerothermodynamic Testing Capabilities—Present and Future. AIAA-90-1376, 1990.

29. Beckwith, I. E.; and Miller, C. G. III: Aerothermodynamics and Transition in High-Speed Wind Tunnels at NASA Langley. *Annual Rev. Fluid Mech.*, Volume 22, Annual Rev. Inc., 1990, pp. 419–439.

30. Miller, Charles G. III: *Experimental and Predicted Heating Distributions for Biconics at Incidence in Air at Mach 10.* NASA TP-2334, 1984.

31. Miller, Charles G. III: *Measured Pressure Distributions, Aerodynamic Coefficients, and Shock Shapes on Blunt Bodies at Incidence in Hypersonic Air and CF_4.* NASA TM-84489, 1982.

32. Meyer, R. F.: *A Note on a Technique of Surface Flow Visualization.* LR-457, Natl. Res. Counc. Canada, 1966. (Available from DTIC as AD 803 514.)

33. Zheng, Chingfa: *Study of Experimental Technique of Oil Flow With Emphasis on Quantitative Determination of the Flow Position Parameters on the Surface.* NASA TT-20341, 1988.

34. Smith, R. E.: *Two-Boundary Grid Generation for the Solution of the Three-Dimensional Compressible Navier-Stokes Equations.* NASA TM-83123, 1981.

35. Roberts, Glyn O.: Computational Meshes for Boundary Layer Problems. *Proceedings of the Second International Conference on Numerical Methods in Fluid Dynamics*, Volume 8 of *Lecture Notes in Physics*, Maurice Holt, ed., Springer-Verlag, 1971, pp. 171–177.

36. Tauber, M. E.: *A Brief Review of Some Mechanisms Causing Boundary Layer Transition at High Speeds.* NASA TM-102834, 1990.

37. Holland, Scott D.: *Experimental Investigation of Generic Three-Dimensional Sidewall-Compression Scramjet Inlets at Mach 6 in Tetrafluoromethane.* NASA TM-4497, 1993.

38. Kubota, H.; and Stollery, J. L.: An Experimental Study of the Interaction Between a Glancing Shock Wave and a Turbulent Boundary Layer. *J. Fluid Mech.*, vol. 116, 1982, pp. 431–458.

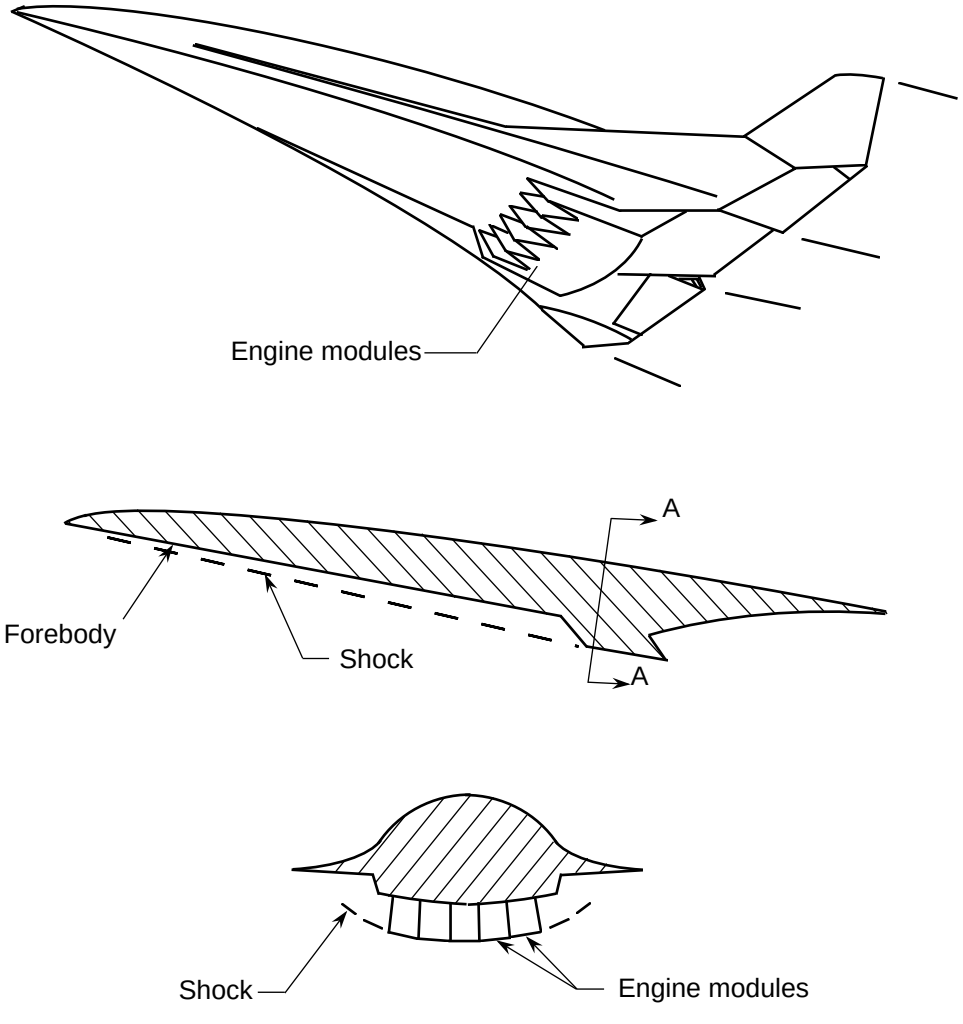

Figure 1. Propulsion airframe integration.

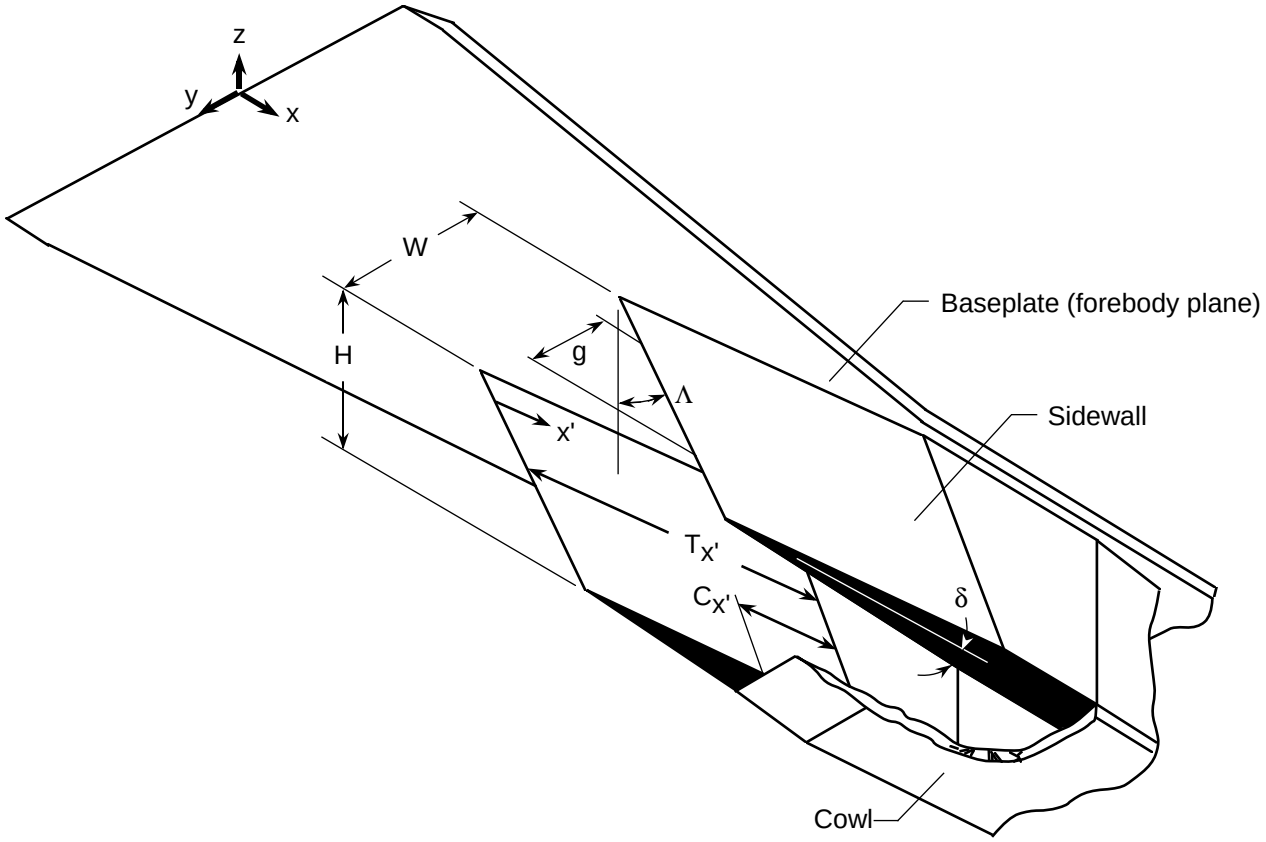

Figure 2. Inlet model shown in flight orientation.

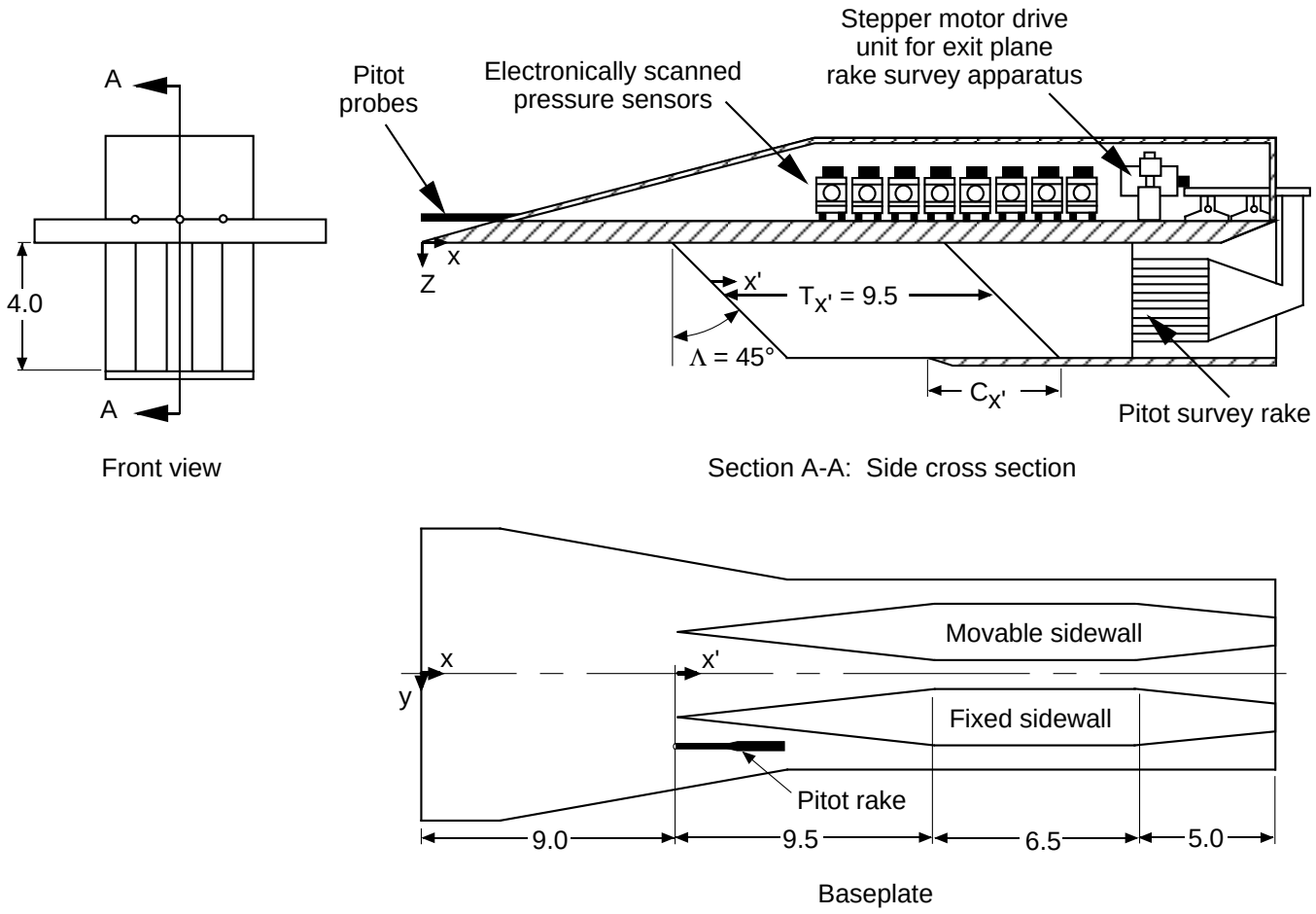

Figure 3. Three-view drawing of inlet configuration. Linear dimensions in inches.

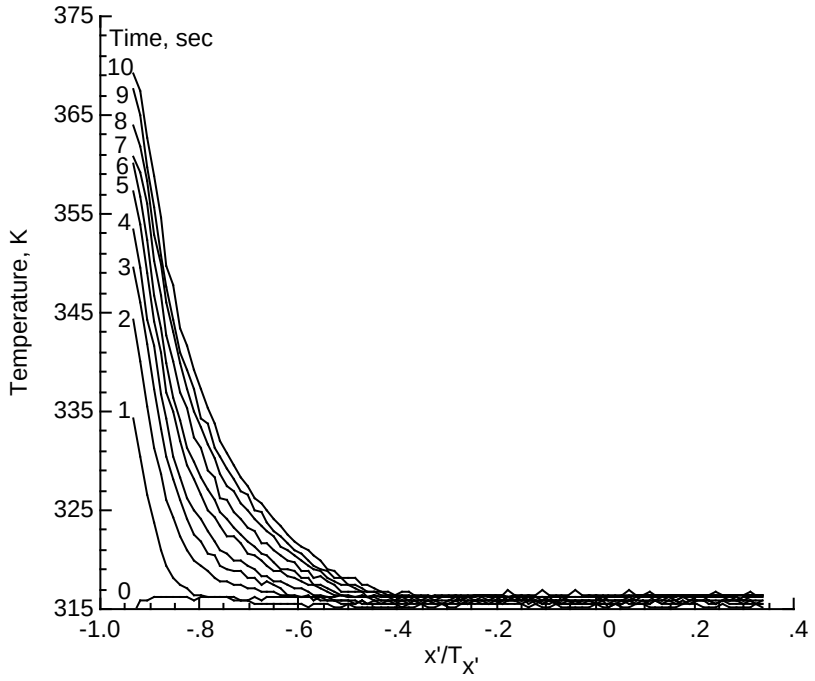

Figure 4. Surface temperature distribution down inlet baseplate centerline. CR = 3; Re = 2.15×10^6 per foot; 0 percent cowl.

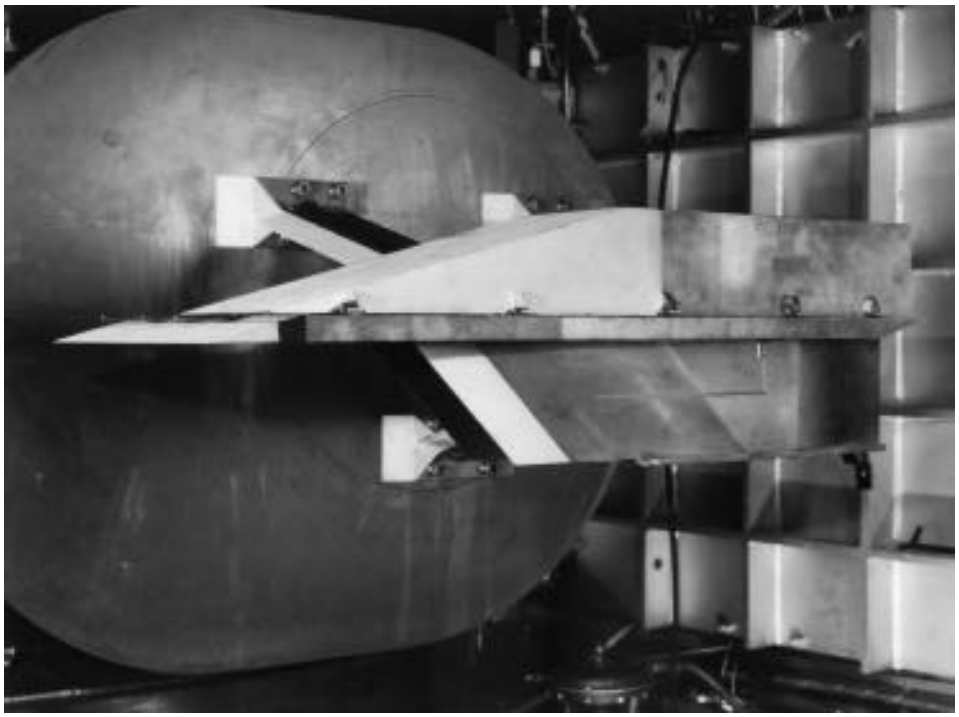

L-90-04394

Figure 5. Photograph of inlet model on injection plate.

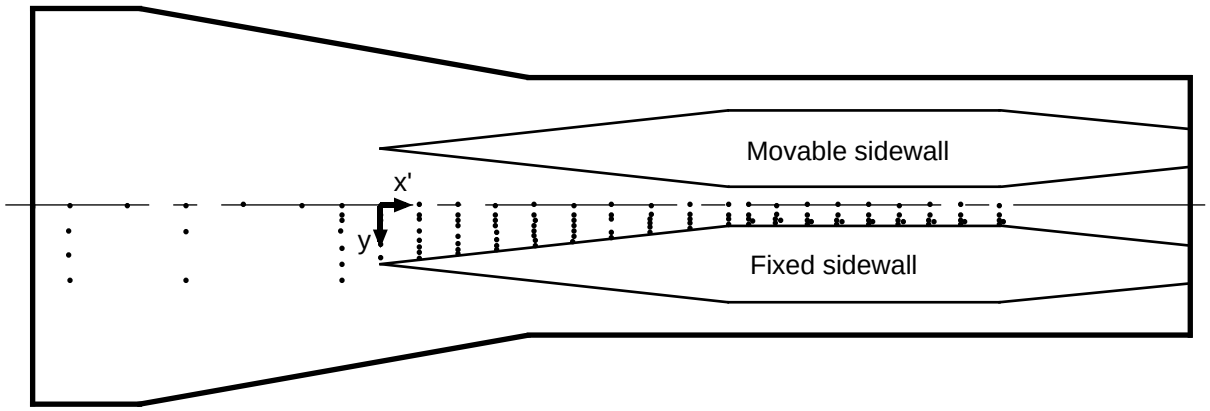

Figure 6. Baseplate orifice locations and coordinate system identification (centerline shown for CR = 3 configuration; orifice size not to scale).

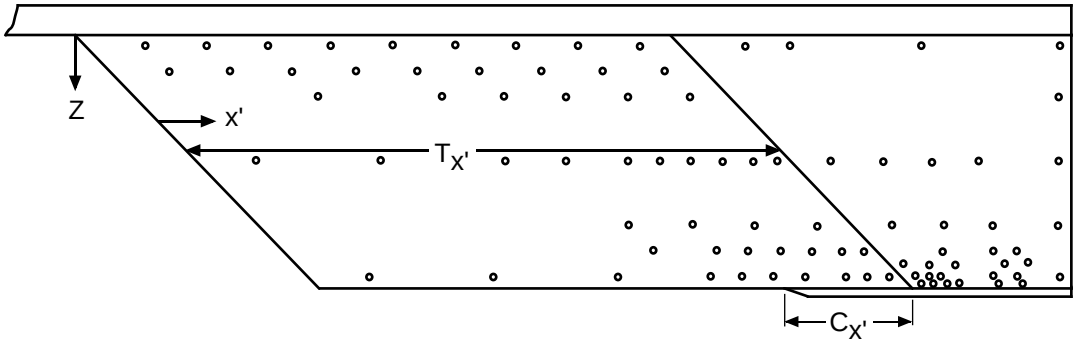

Figure 7. Sidewall orifice locations and identification of coordinate system (orifice size not to scale).

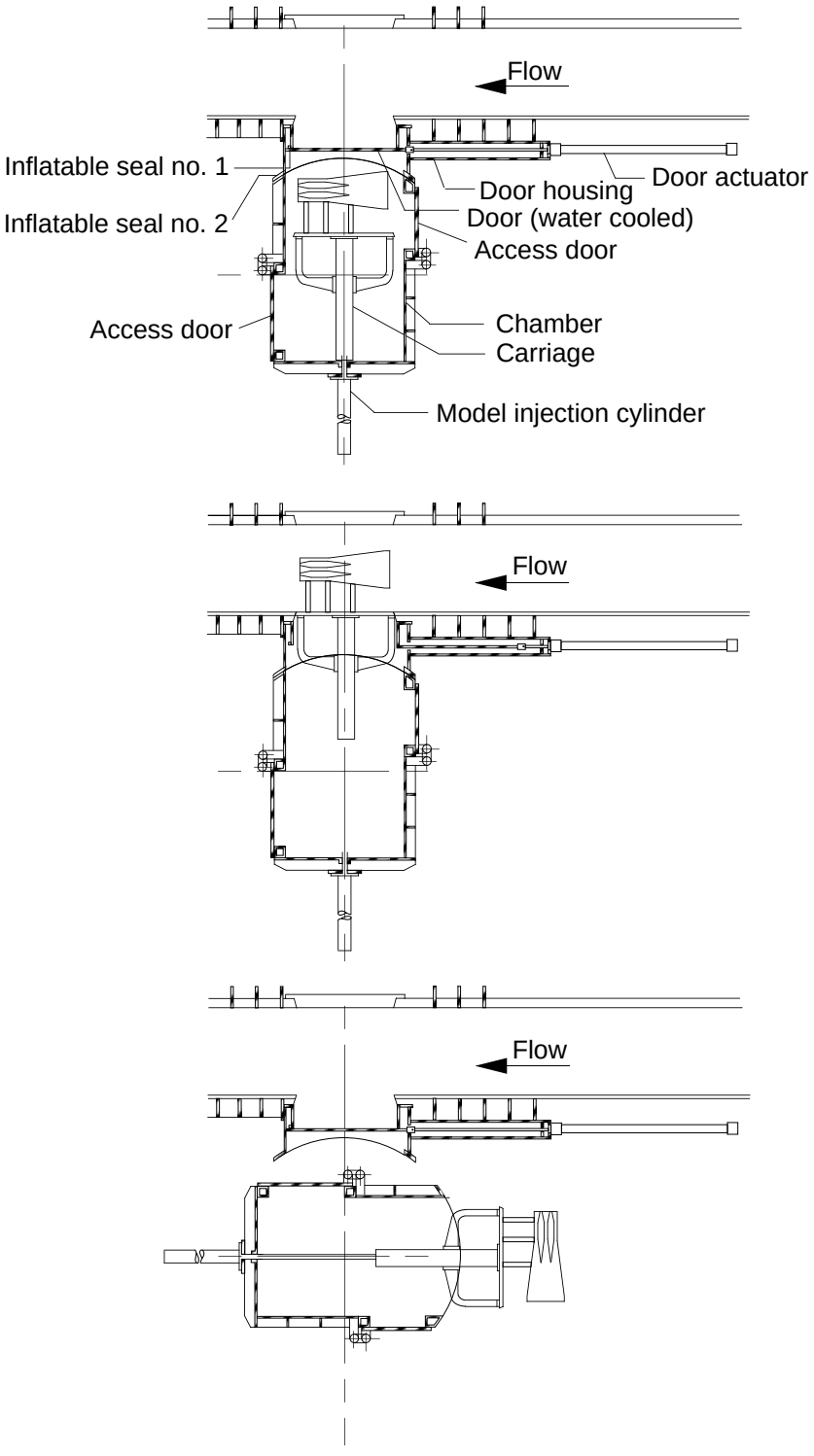

Figure 8. Model injection sequence, showing model retracted prior to injection, model injected into the tunnel, and model injected into work area.

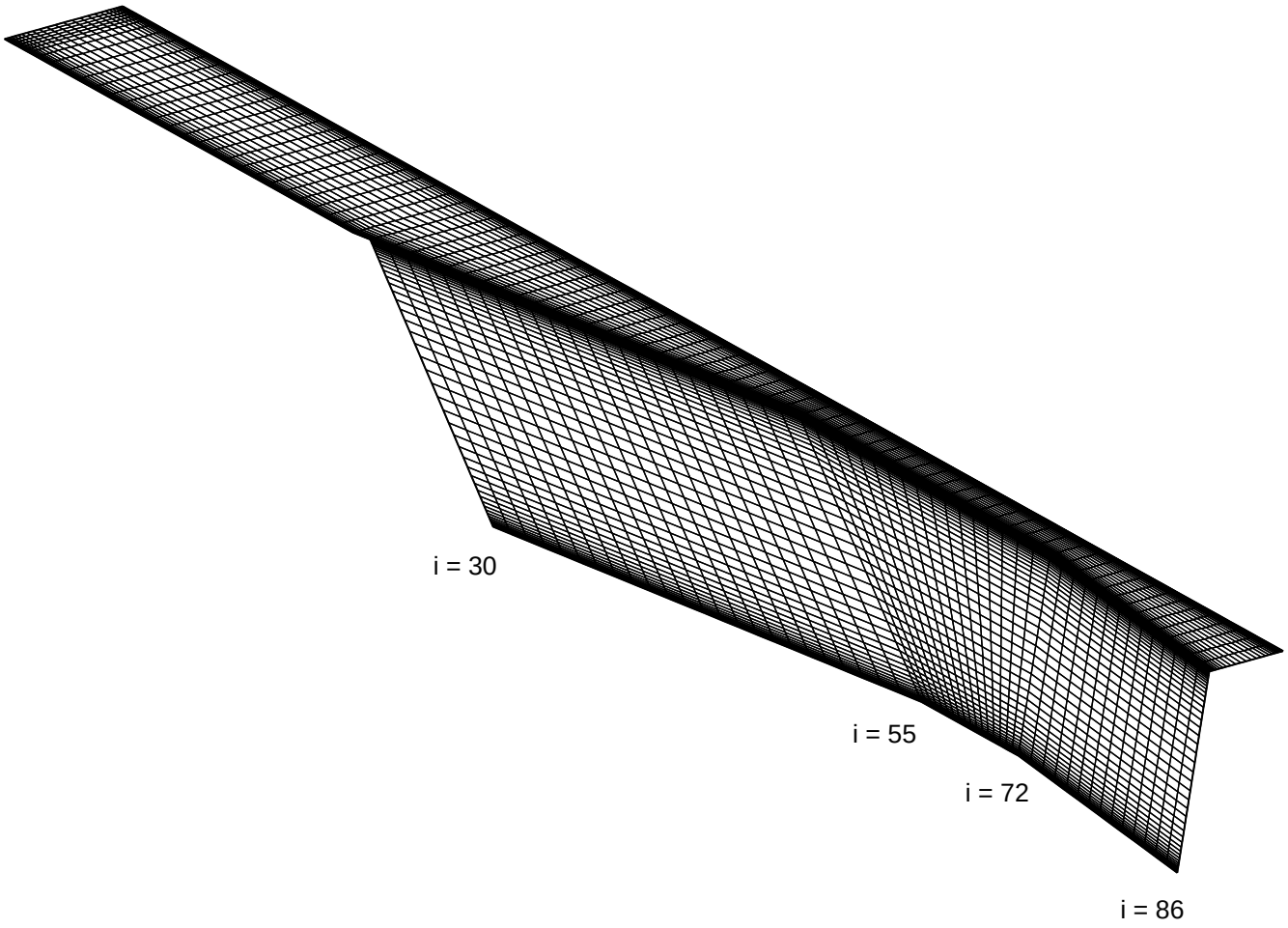

Figure 9. Computational grid of inlet sidewall and baseplate surfaces. (Lateral scale expanded by a factor of 2 for clarity.)

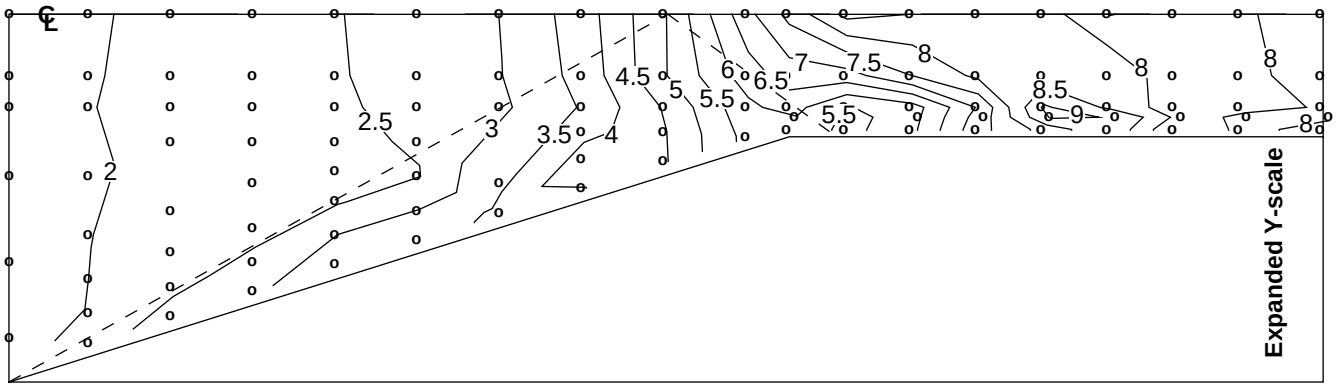

(a) Baseplate; run 66.

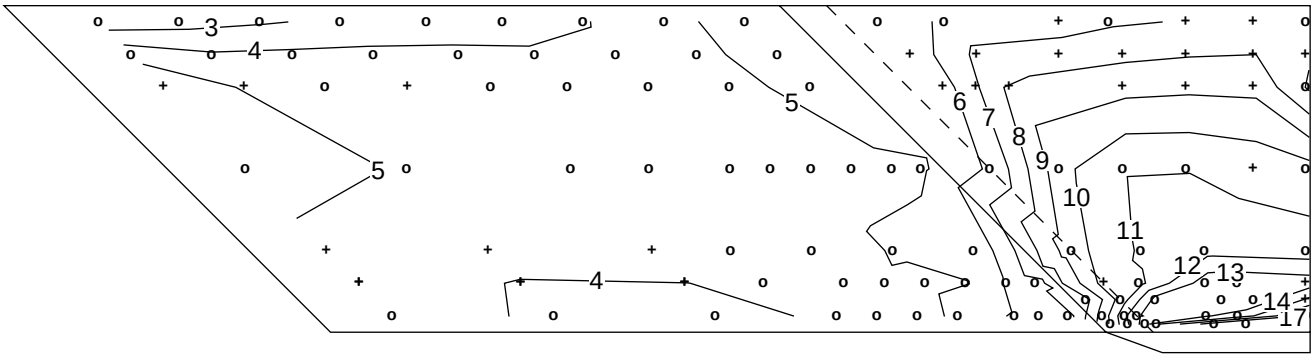

(b) Sidewall; run 66.

Figure 10. p/p_∞ contours. CR = 3; Re = 2.15×10^6 per foot; 0 percent cowl.

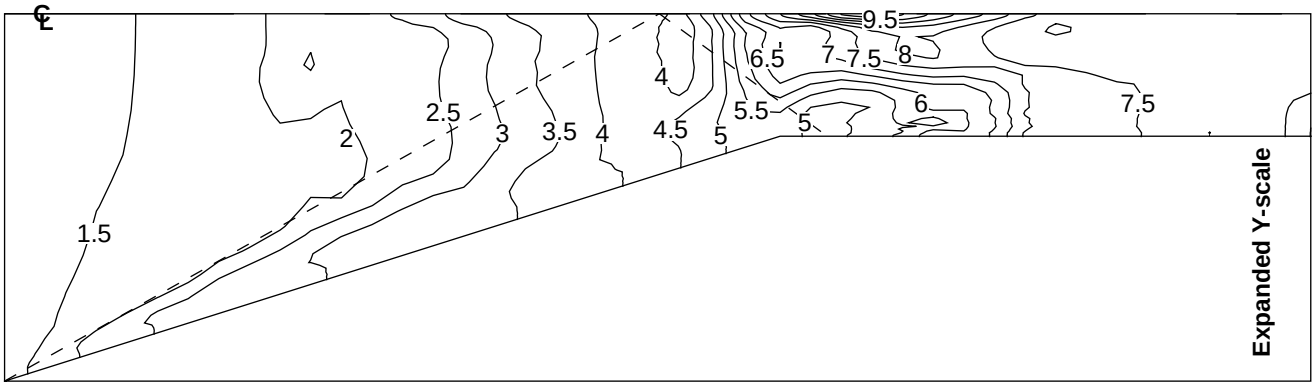

(c) Computed baseplate.

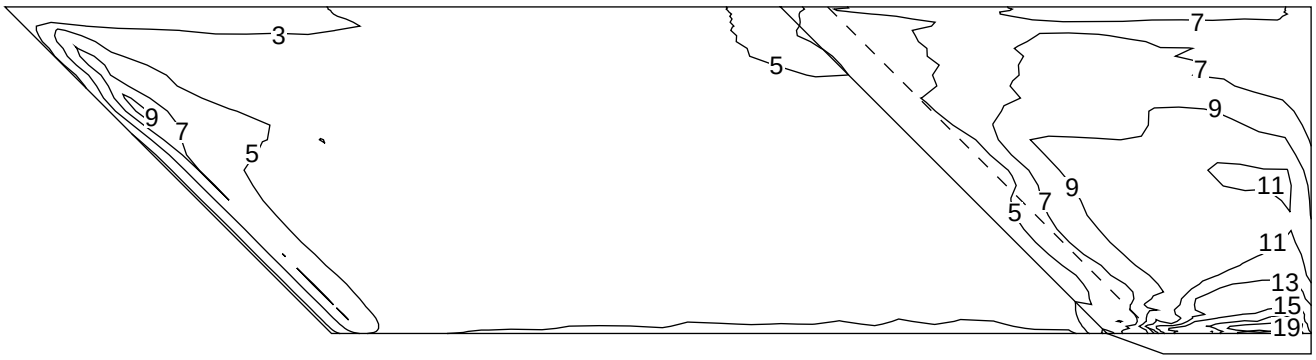

(d) Computed sidewall.

Figure 10. Concluded.

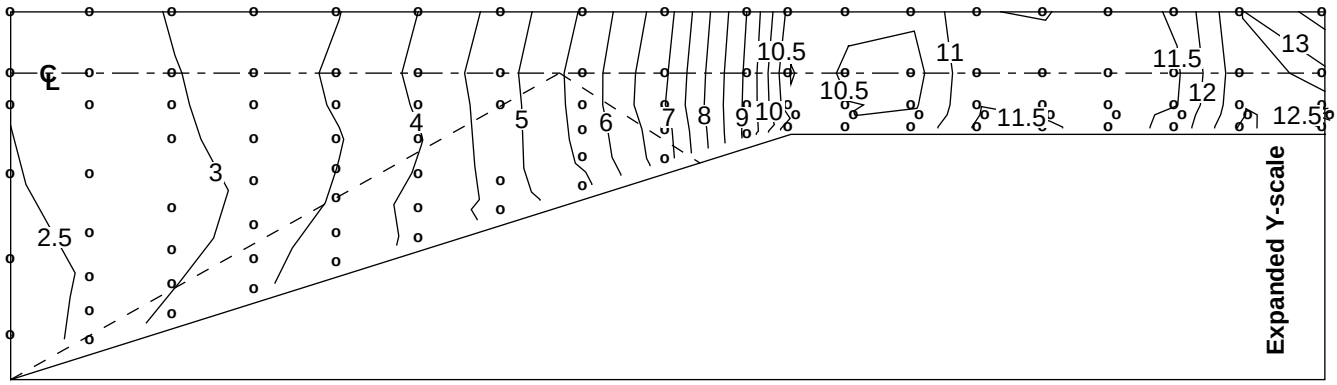

(a) Baseplate.

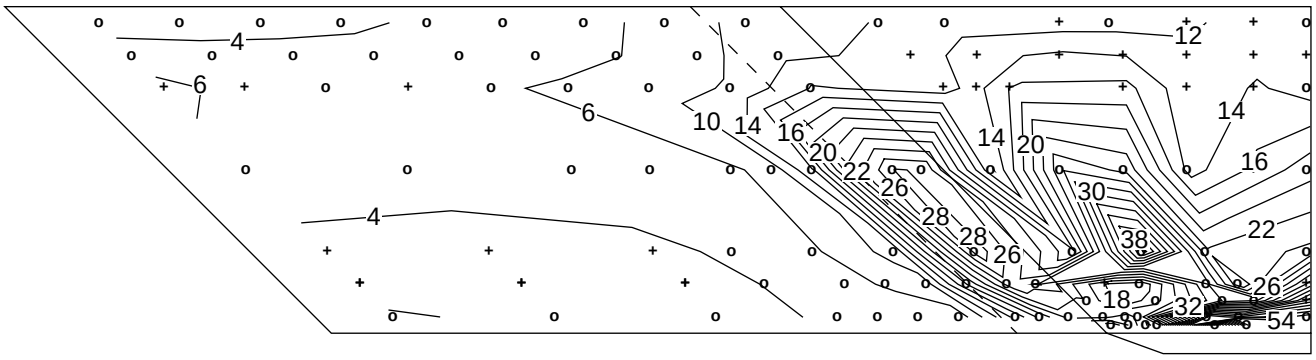

(b) Sidewall.

Figure 11. p/p_∞ contours. CR = 5; Re = 2.15×10^6 per foot; 0 percent cowl; run 46.

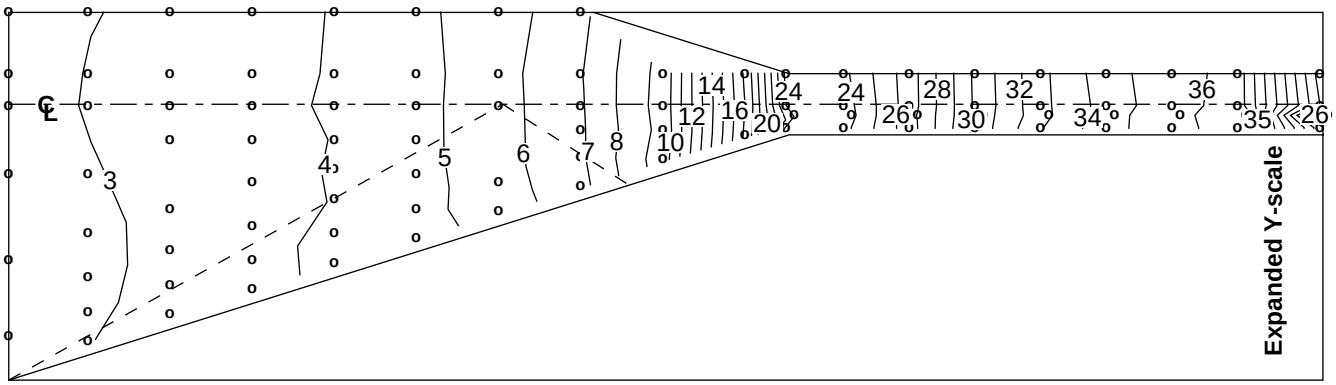

(a) Baseplate.

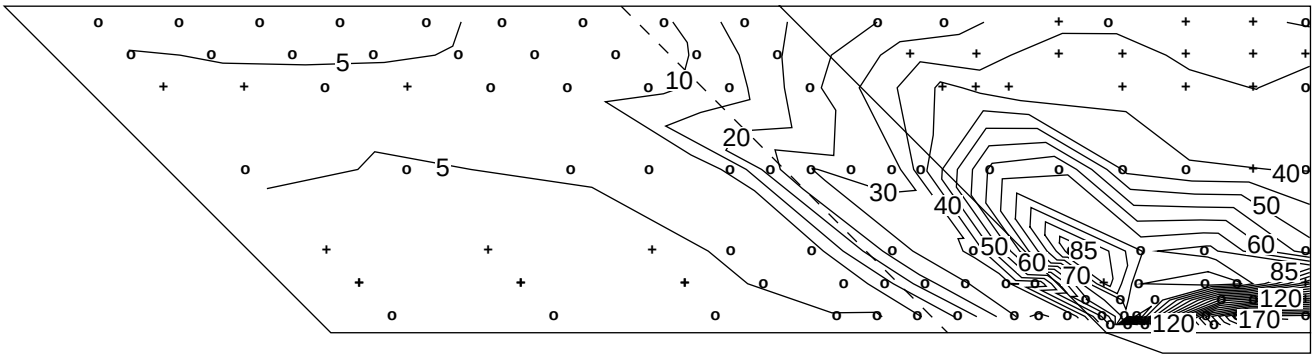

(b) Sidewall.

Figure 12. p/p_∞ contours. CR = 9; Re = 2.15×10^6 per foot; 0 percent cowl; run 49.

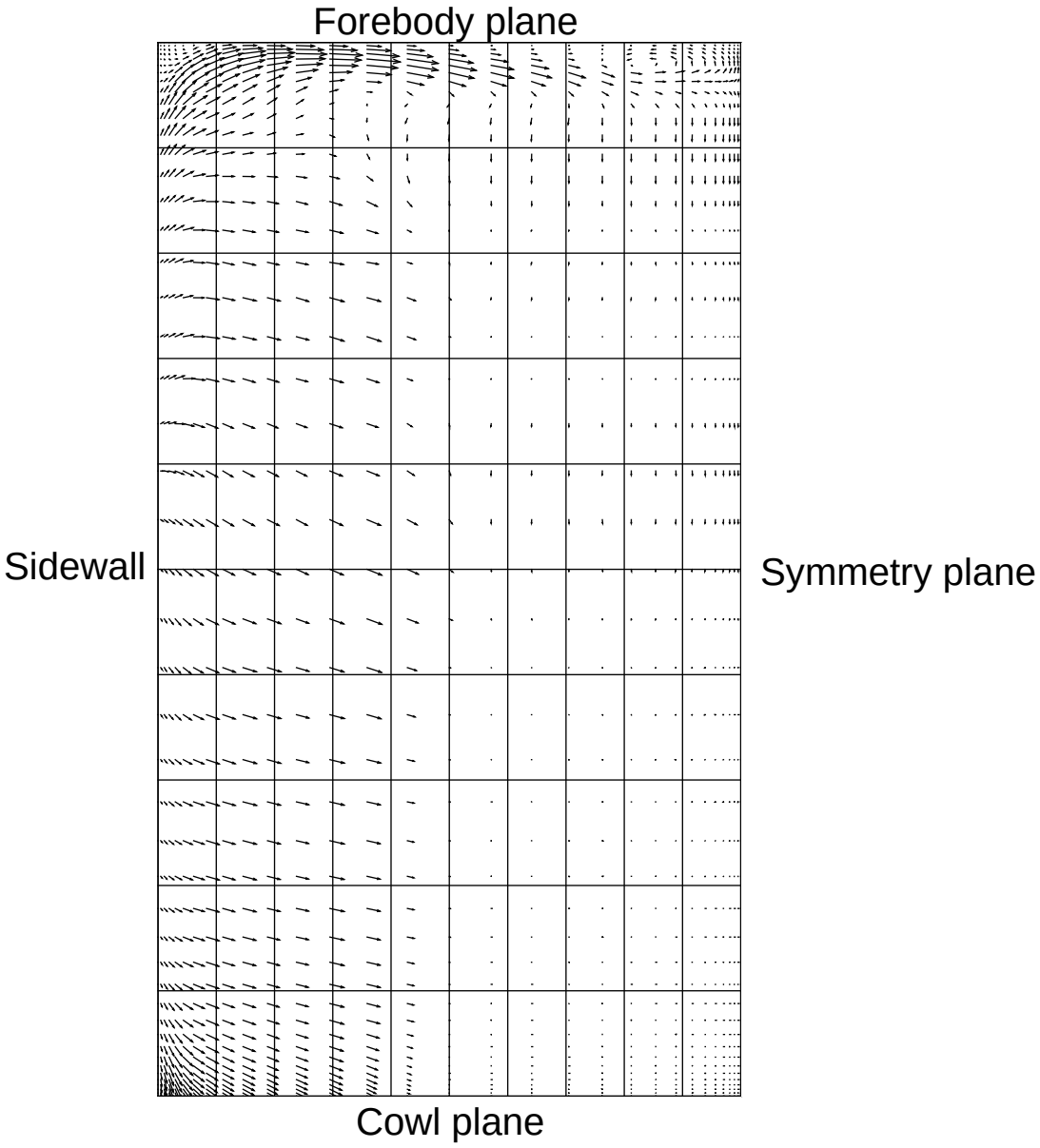

Figure 13. Cross-flow velocity vectors at $i = 40$ and $x'/T_{x'} = 0.40$. CR = 3; 0 percent cowl; Re = 2.15×10^6 per foot.

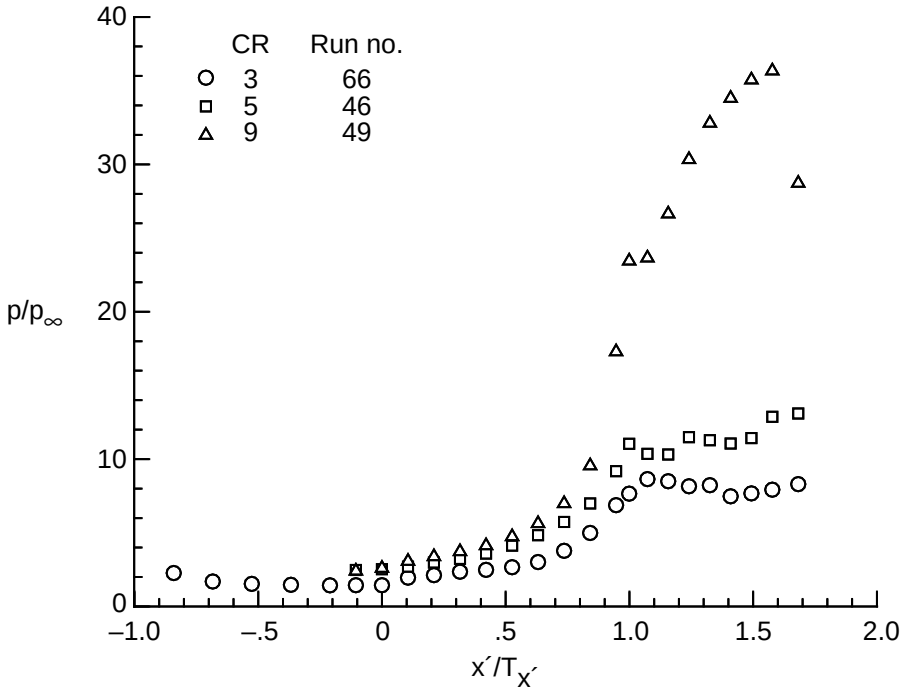

(a) Centerline pressures. CR = 3, 5, and 9.

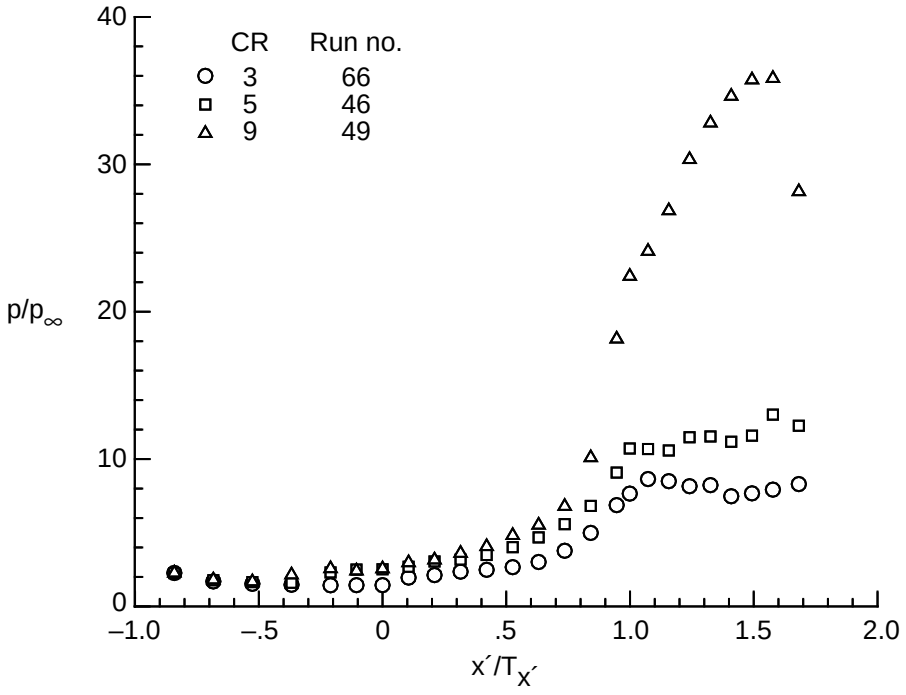

(b) Pressures along CR = 3 centerline orifices.

Figure 14. Contraction ratio effects. Re = 2.15×10^6 per foot; 0 percent cowl.

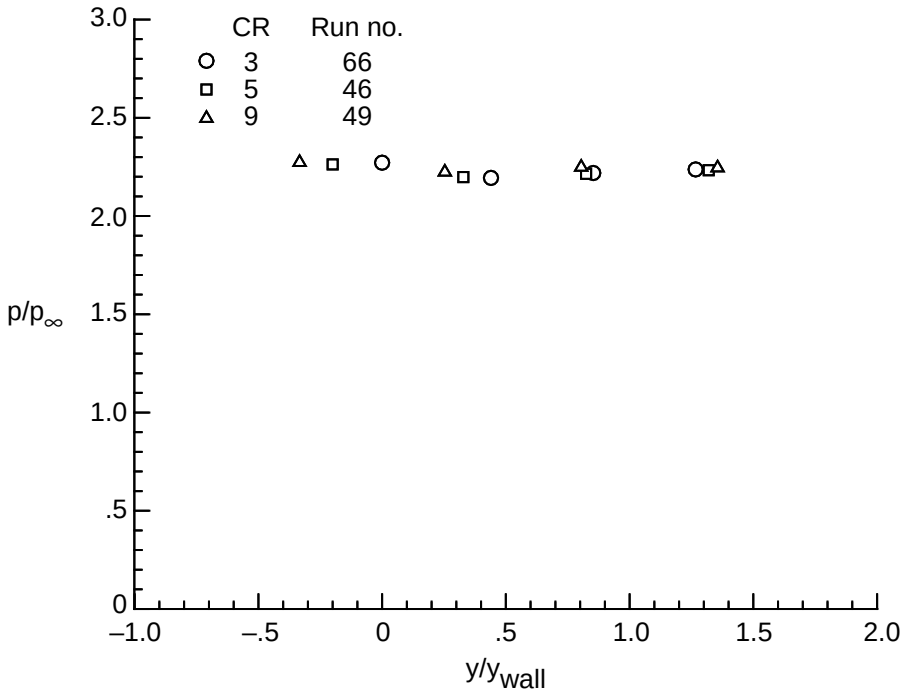

(c) Baseplate pressures. $x'/T_{x'} = -0.8412$.

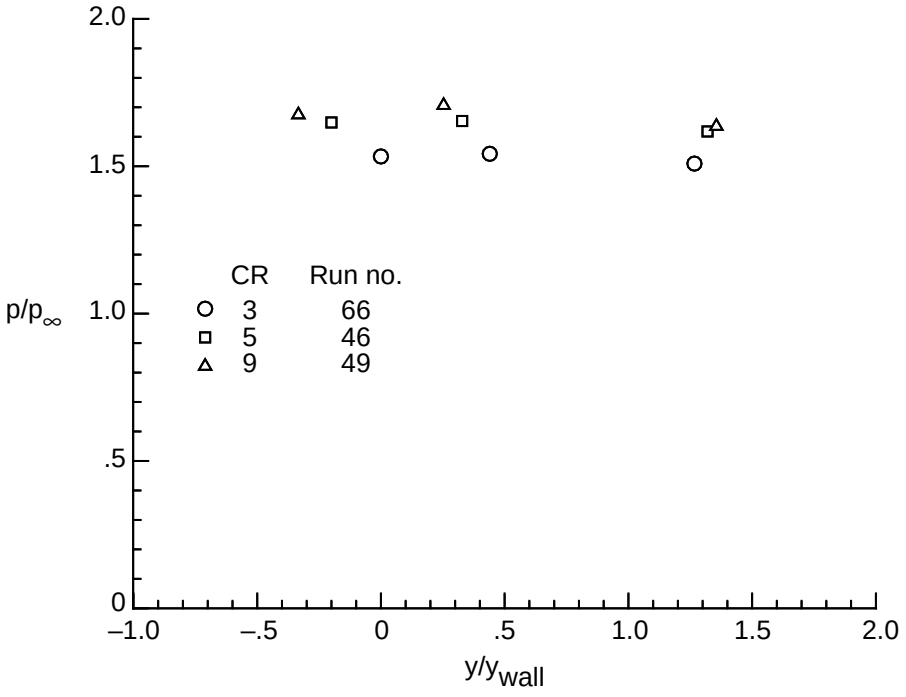

(d) Baseplate pressures. $x'/T_{x'} = -0.5258$.

Figure 14. Continued.

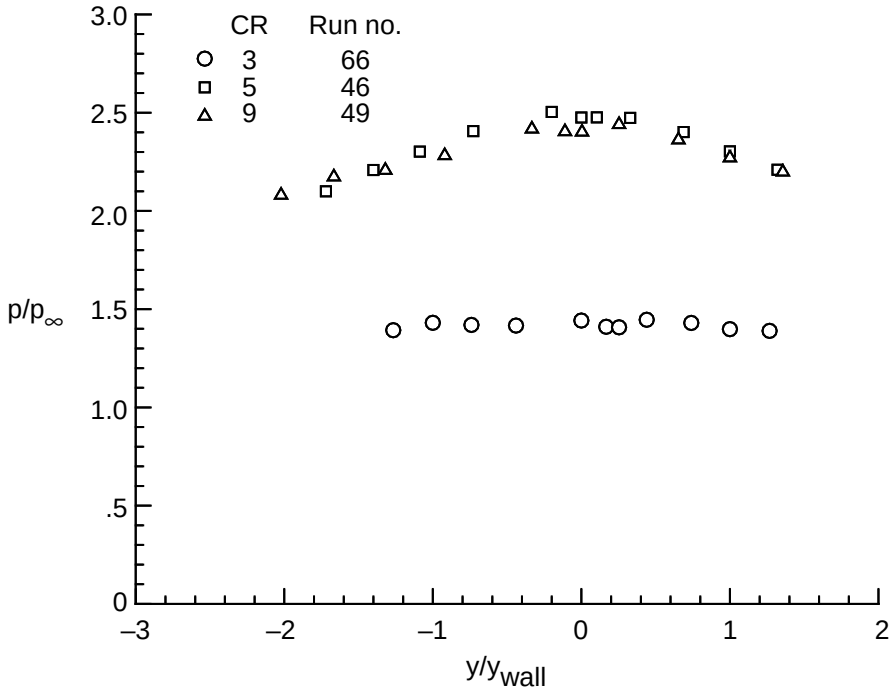

(e) Baseplate pressures. $x'/T_{x'} = -0.1052$.

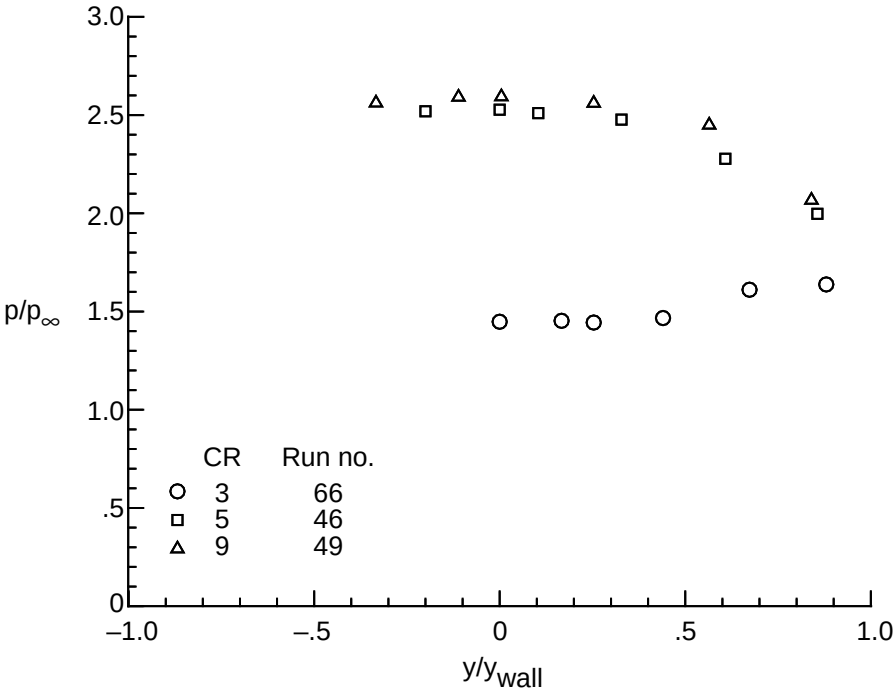

(f) Baseplate pressures. $x'/T_{x'} = 0$.

Figure 14. Continued.

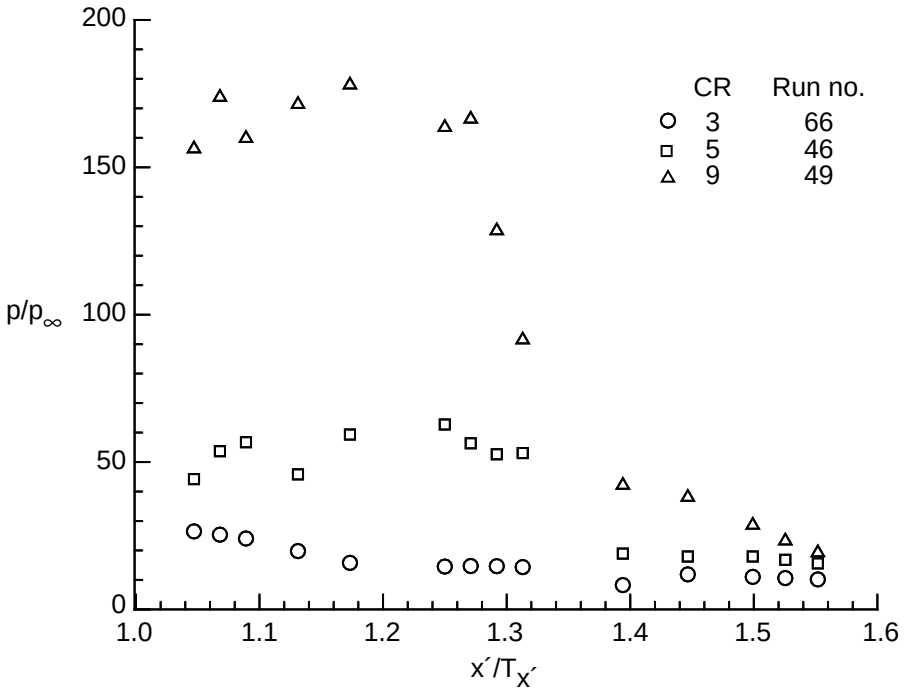

(g) Cowl pressures.

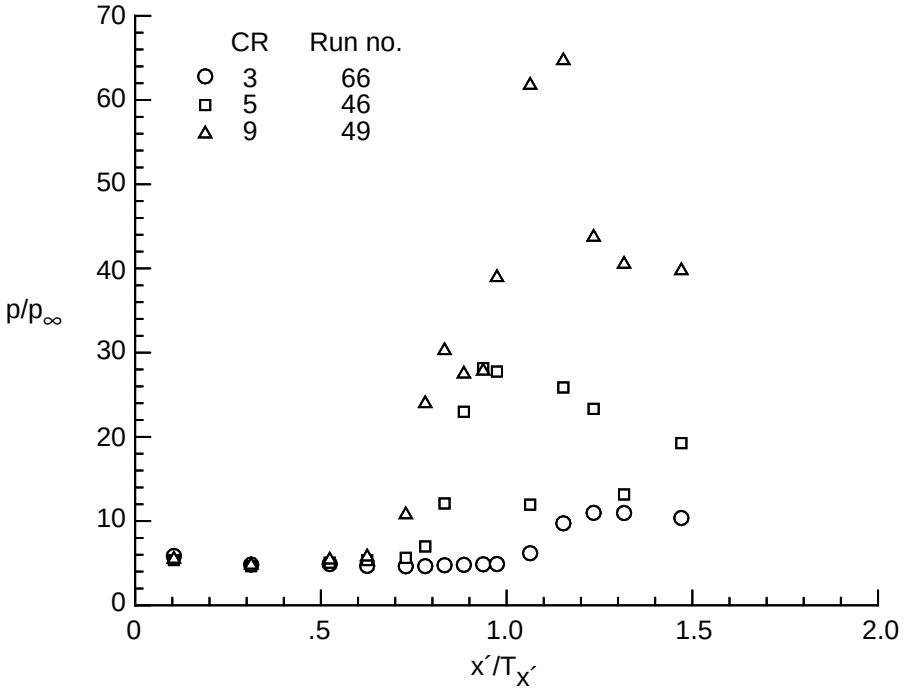

(h) Sidewall centerline pressures. $Z/H = 0.5$.

Figure 14. Concluded.

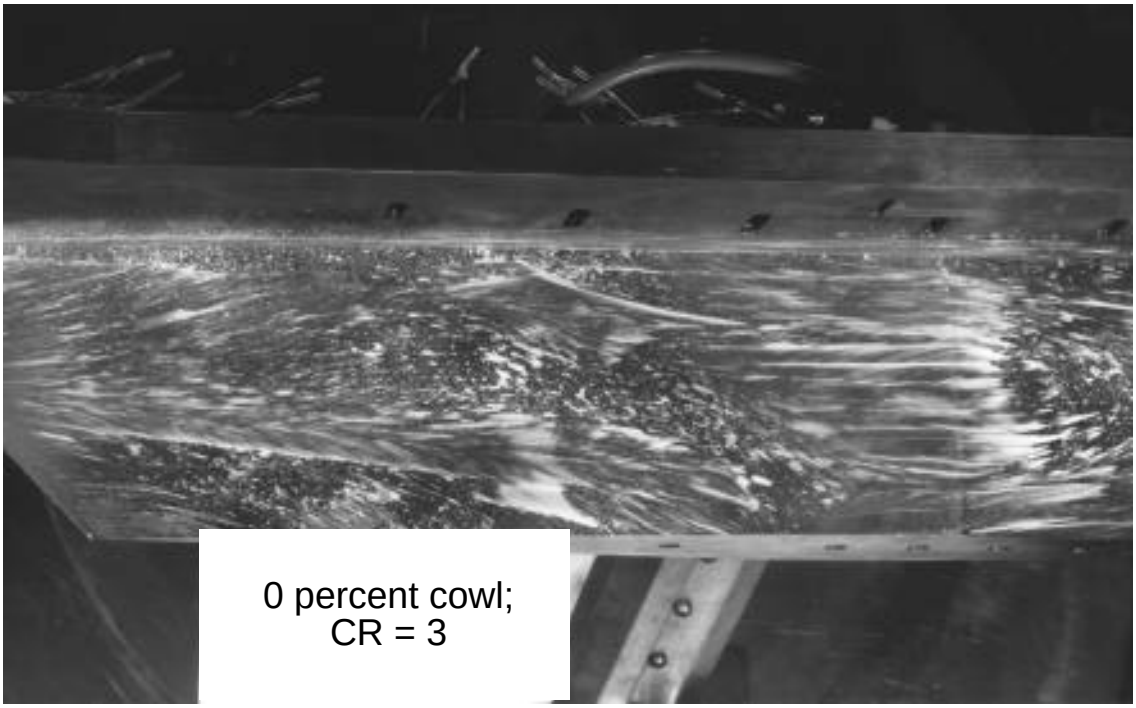

(a) Inlet sidewall. CR = 3.

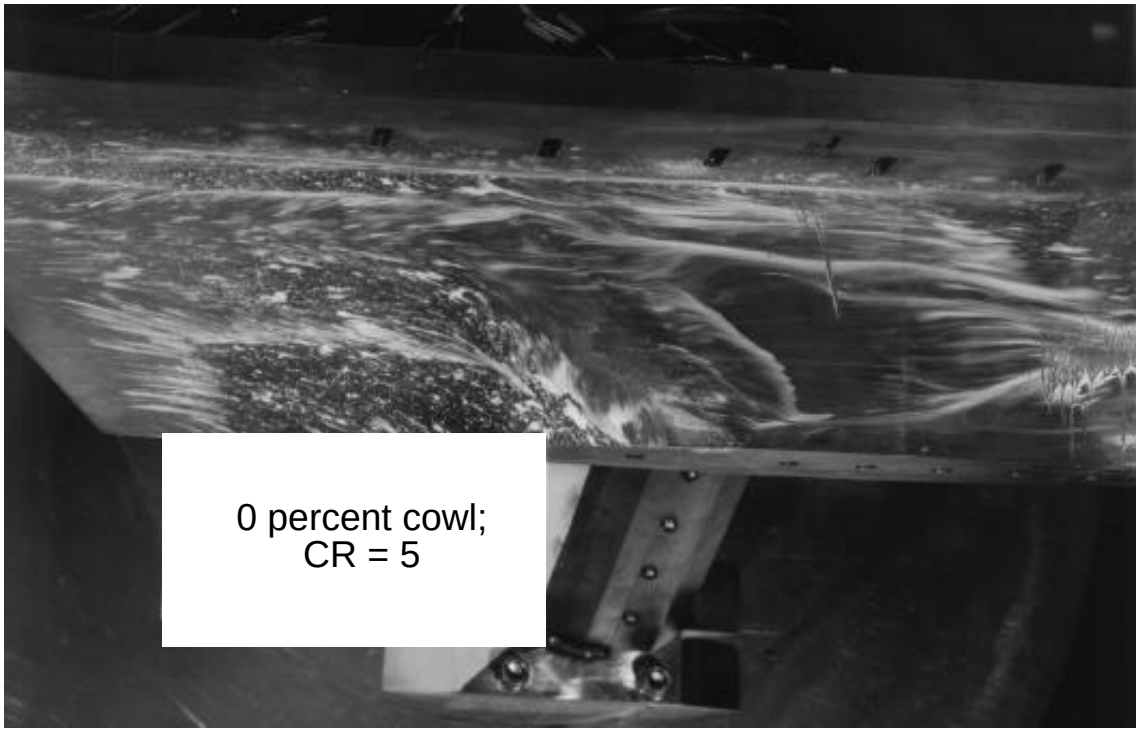

(b) Inlet sidewall. CR = 5.

Figure 15. Oil flow photographs. Re = 2.15×10^6 per foot; 0 percent cowl.

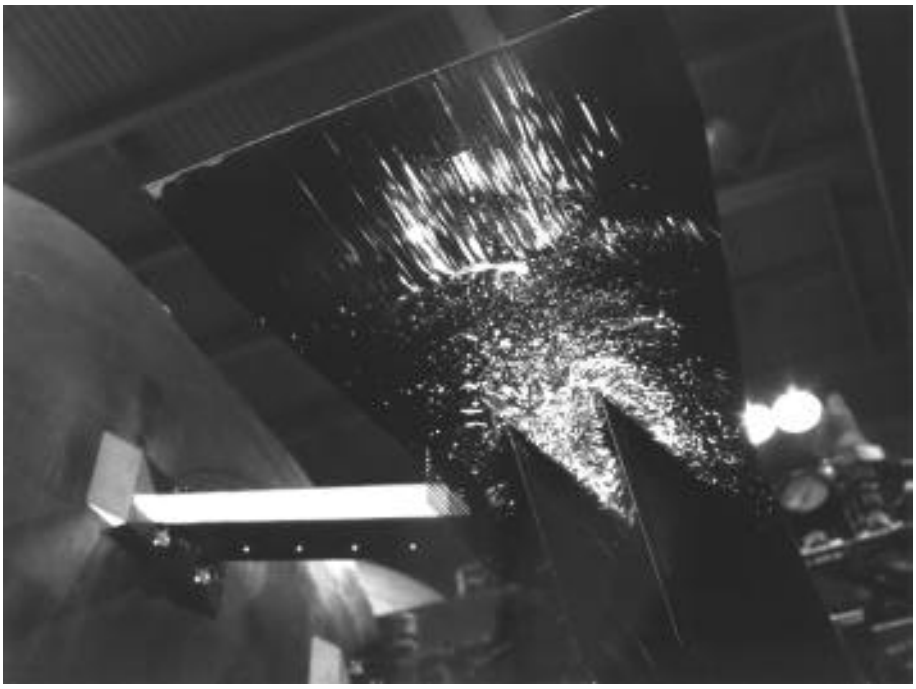

(c) Baseplate, showing forward extent of separation. CR = 9.

(d) Baseplate, showing oil streaks exiting front of inlet and spilling around sidewalls. CR = 9.

Figure 15. Continued.

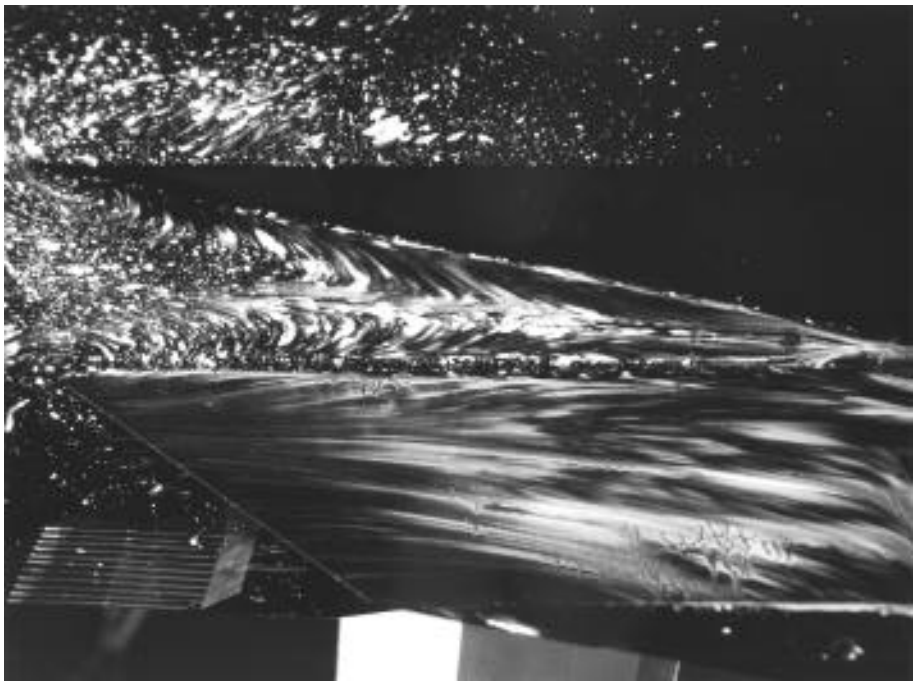

(e) Close-up of baseplate and sidewall. CR = 9.

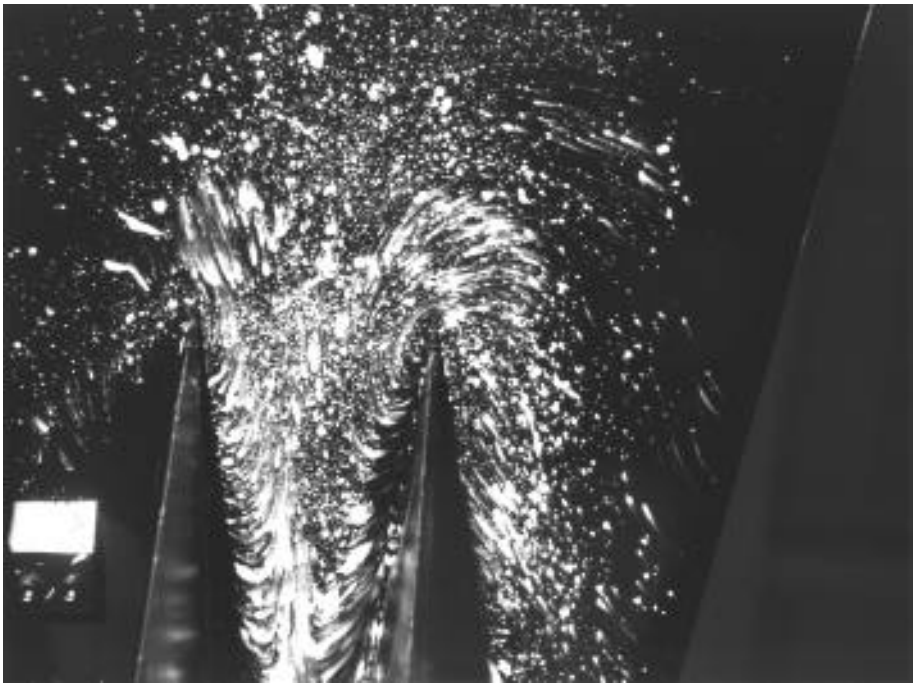

(f) Close-up of baseplate showing oil streaks exiting front of inlet and spilling around sidewalls. CR = 9.

Figure 15. Concluded.

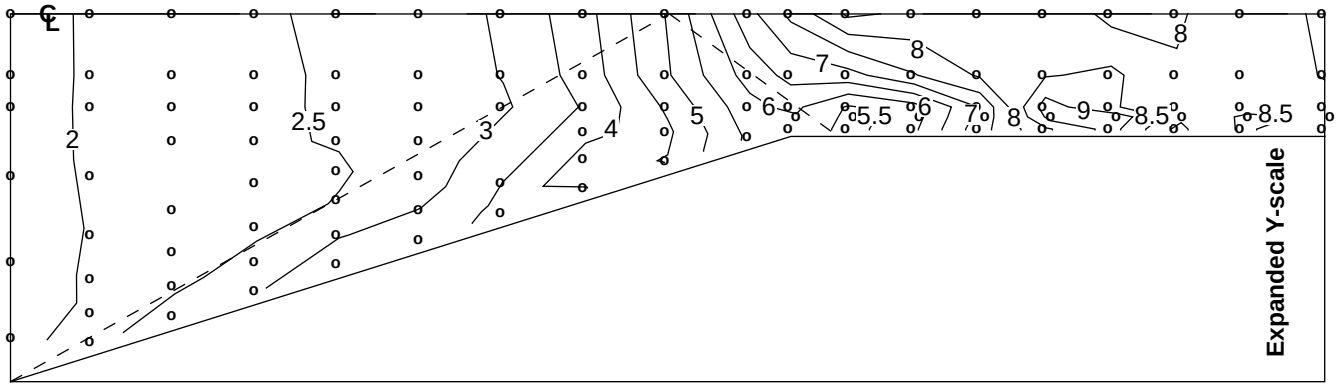

(a) Baseplate; run 60.

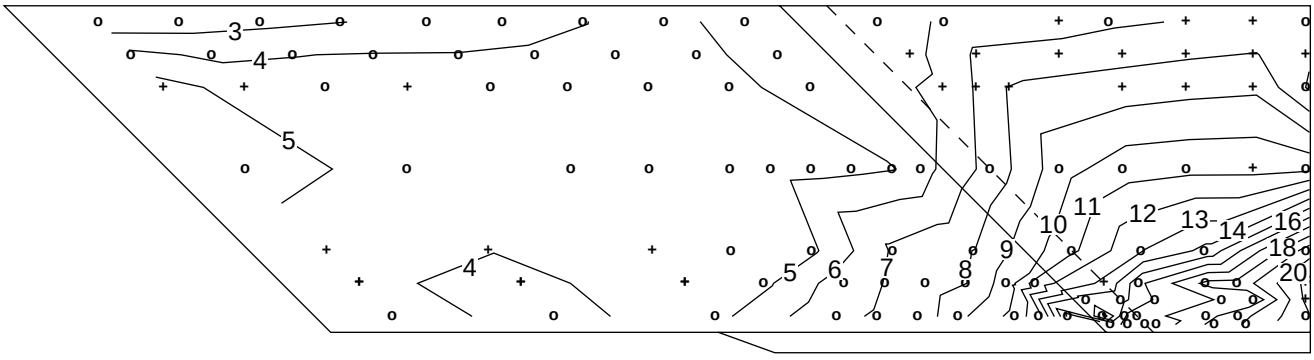

(b) Sidewall; run 60.

Figure 16. p/p_∞ contours. CR = 3; Re = 2.15×10^6 per foot; 50 percent cowl.

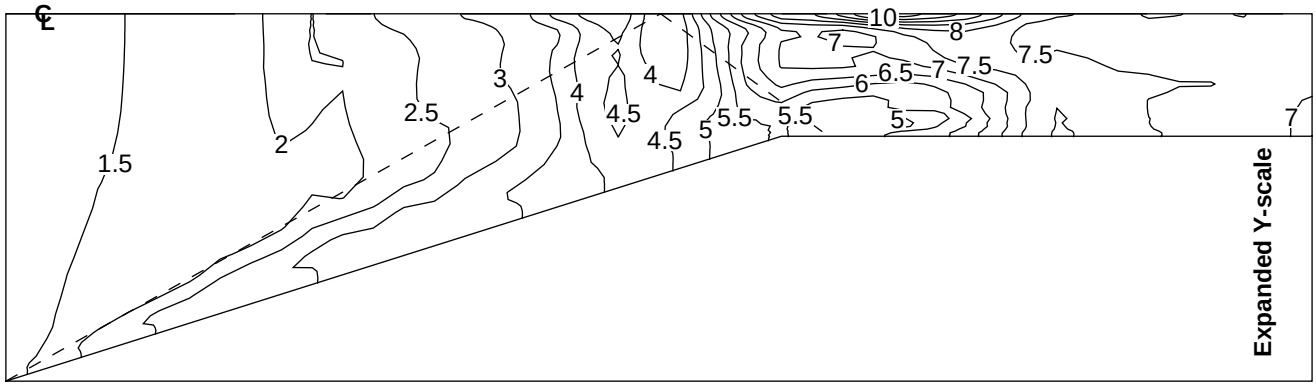

(c) Computed baseplate.

(d) Computed sidewall.

Figure 16. Concluded.

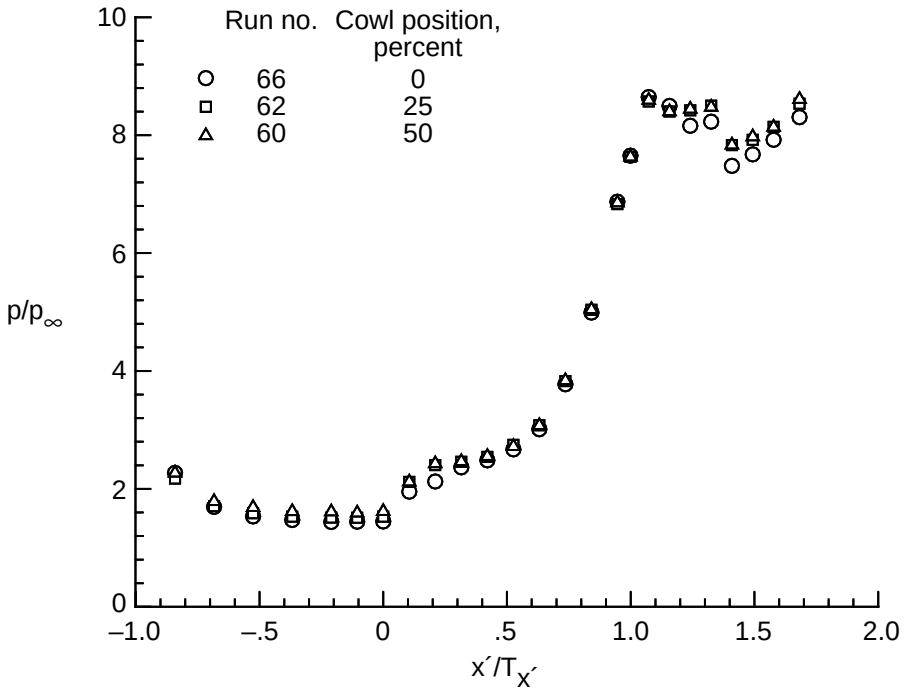

(a) Centerline pressures.

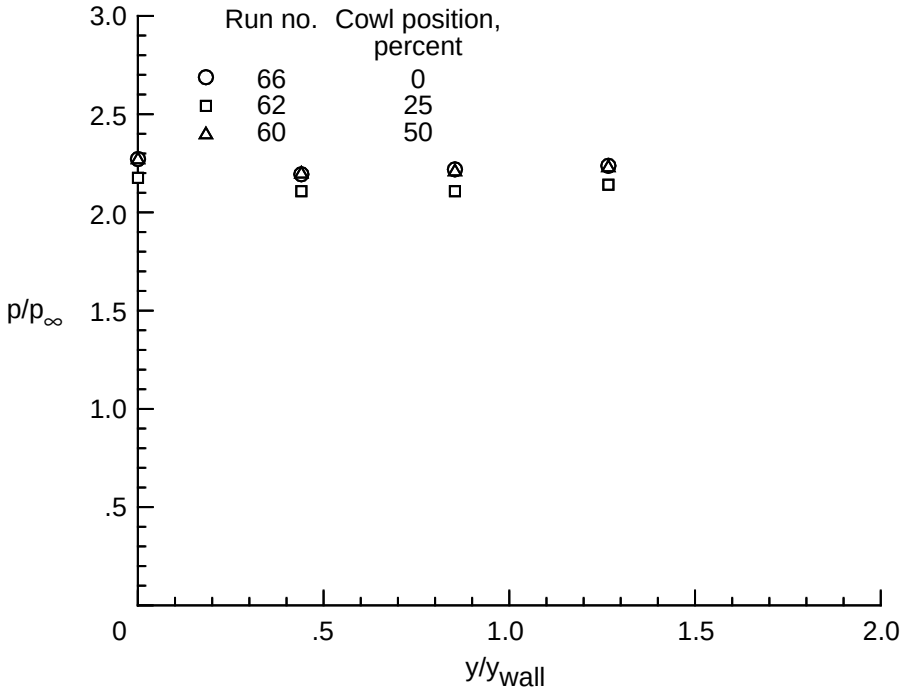

(b) Baseline pressures. $x'/T_{x'} = -0.8412$.

Figure 17. Effect of cowl position on pressure distributions. CR = 3; Re = 2.15 × 10^6 per foot.

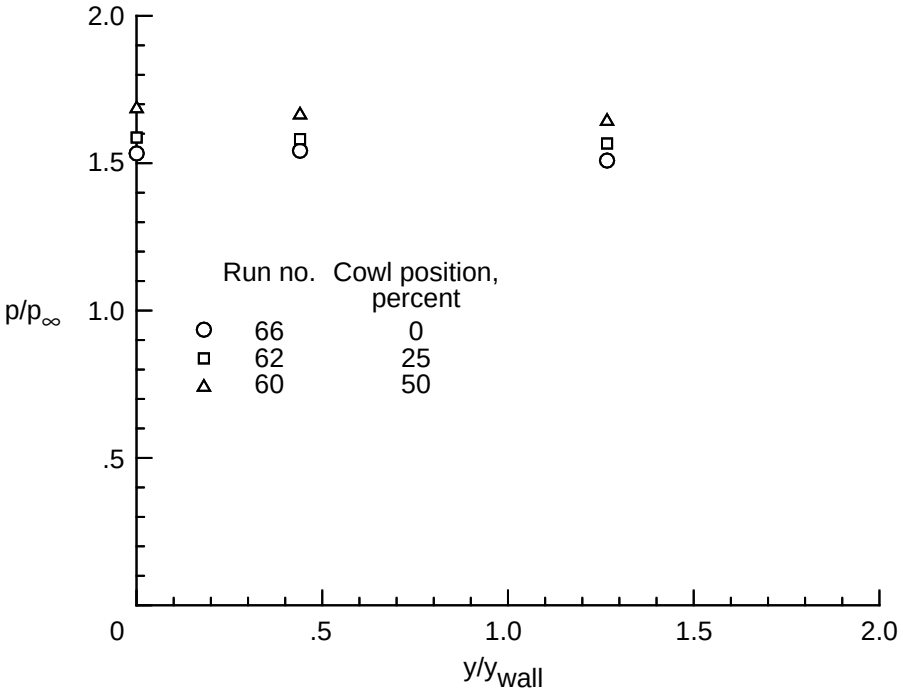

(c) Baseplate pressures. $x'/T_{x'} = -0.5258$.

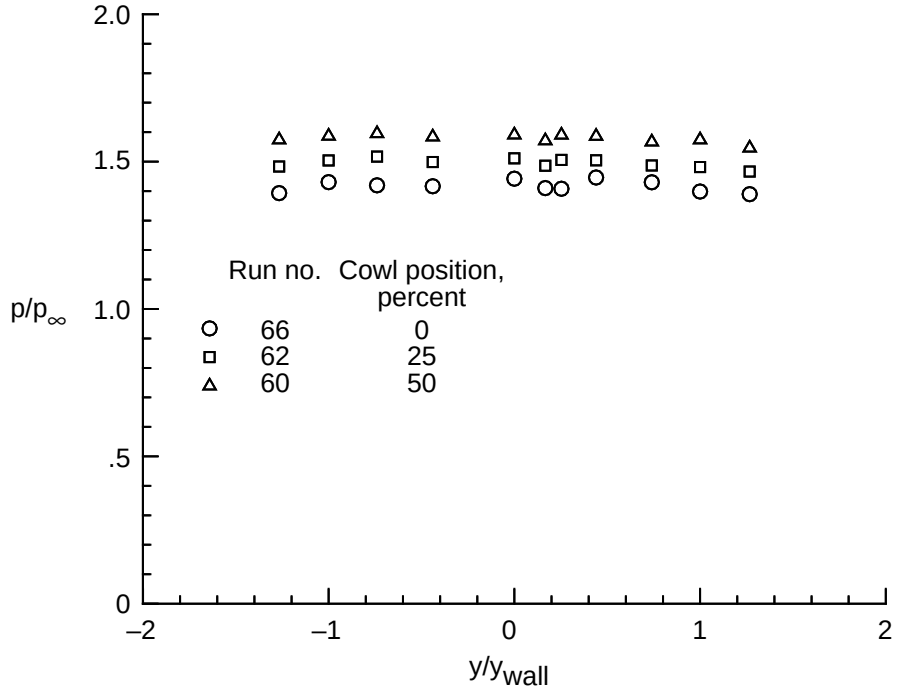

(d) Baseplate pressures. $x'/T_{x'} = -0.1052$.

Figure 17. Continued.

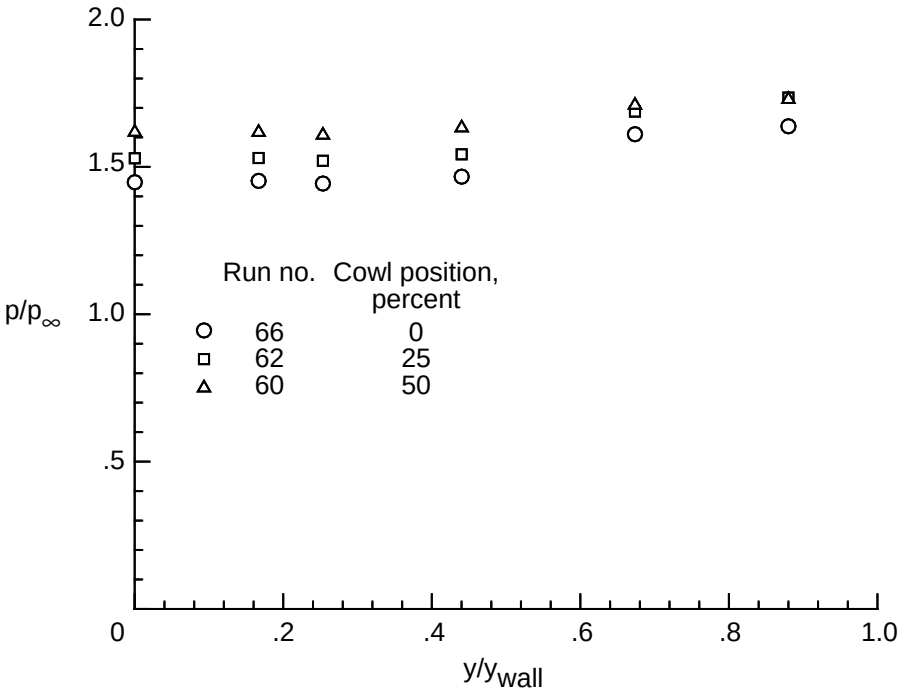

(e) Baseplate pressures. $x'/T_{x'} = 0$.

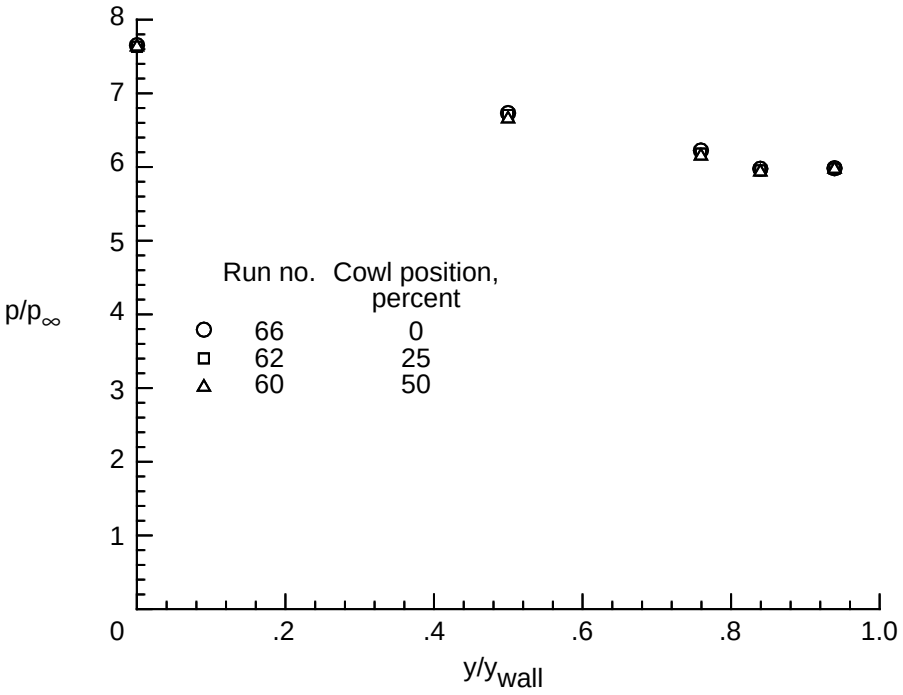

(f) Baseplate pressures. $x'/T_{x'} = 1$.

Figure 17. Continued.

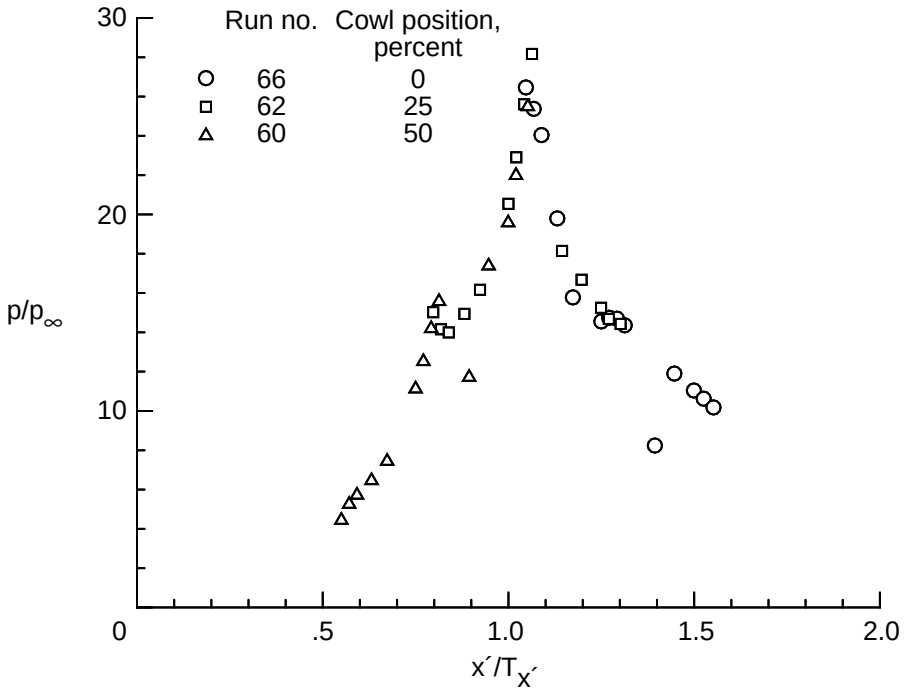

(g) Cowl pressures.

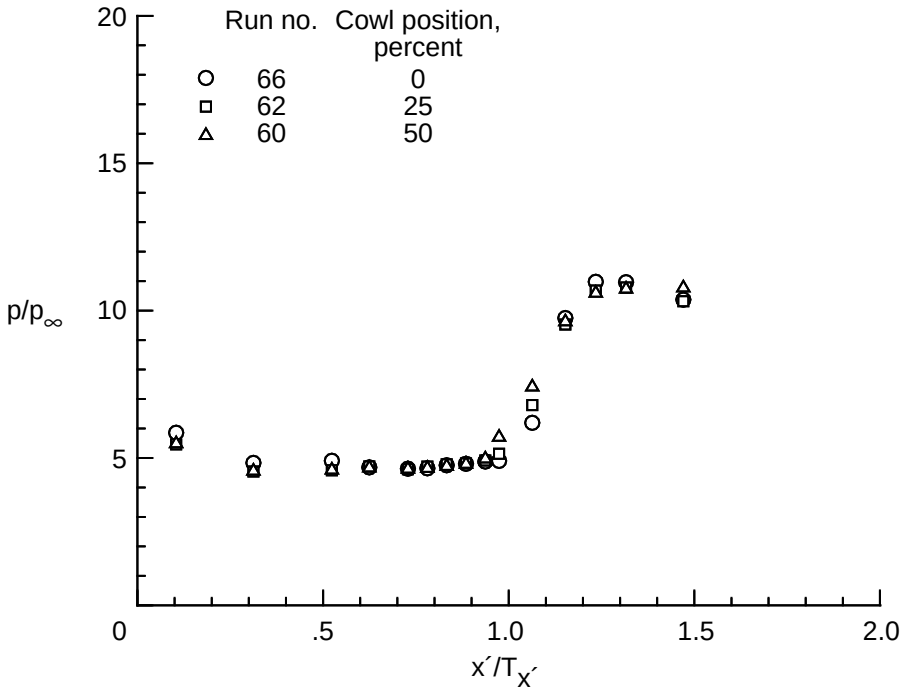

(h) Sidewall centerline pressures. $Z/H = 0.5$.

Figure 17. Concluded.

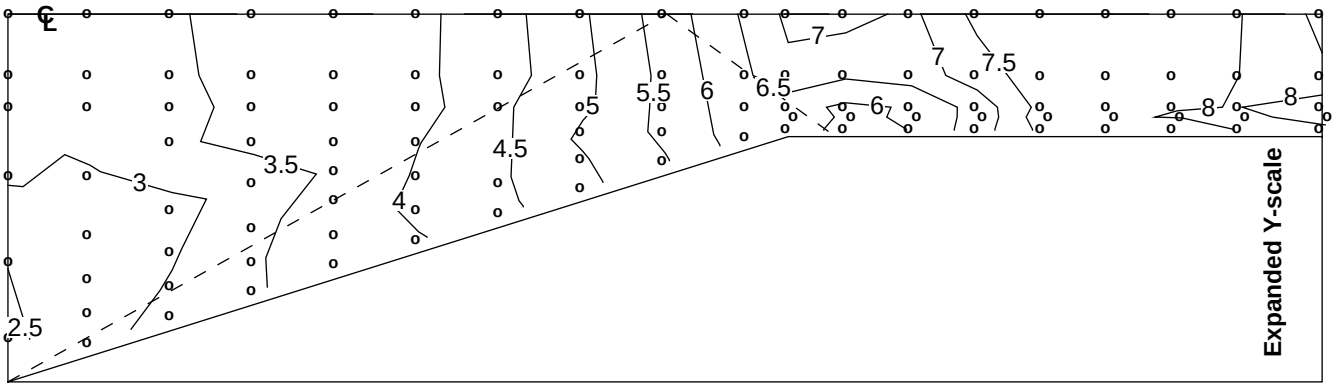

(a) Baseplate.

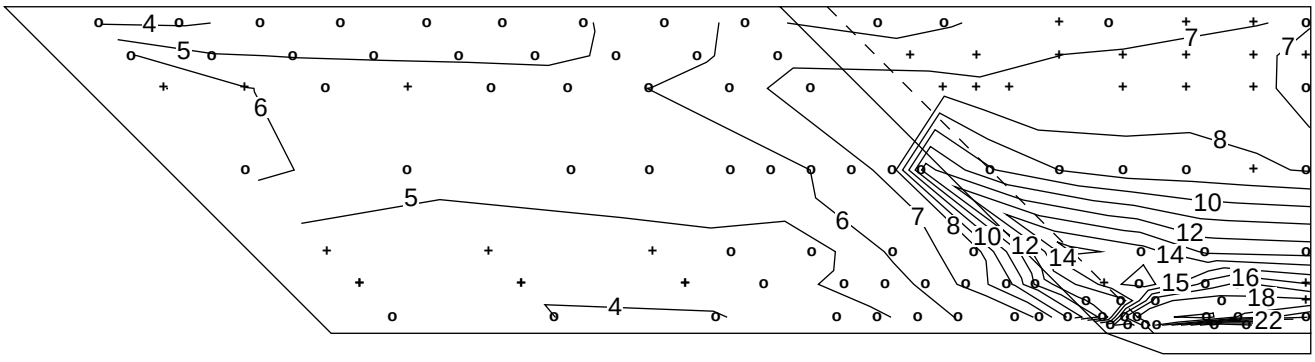

(b) Sidewall.

Figure 18. p/p_∞ contours. CR = 3; Re = 0.55×10^6 per foot; 0 percent cowl; run 64.

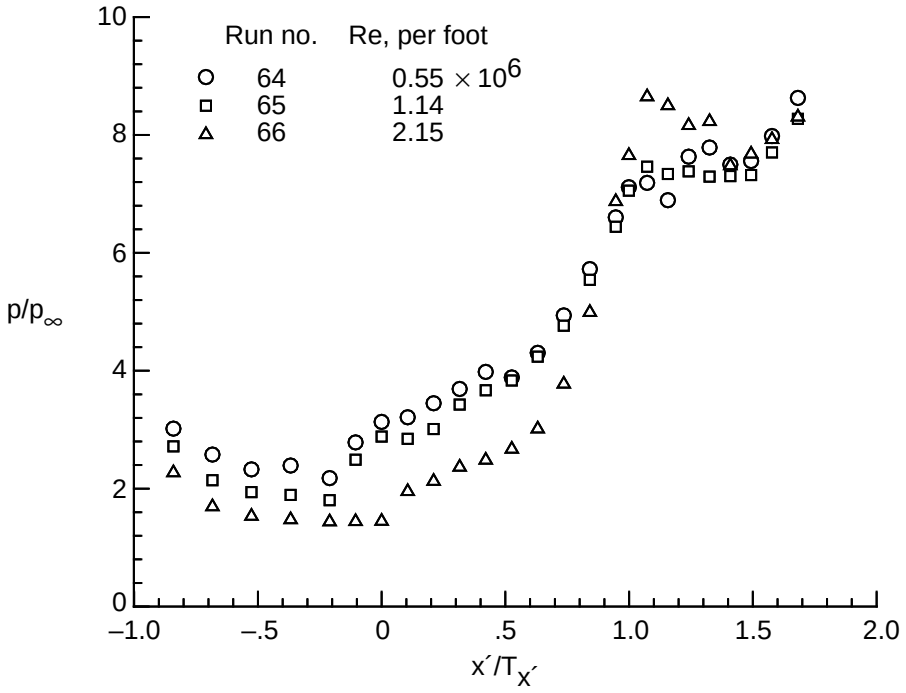

(a) Centerline pressures.

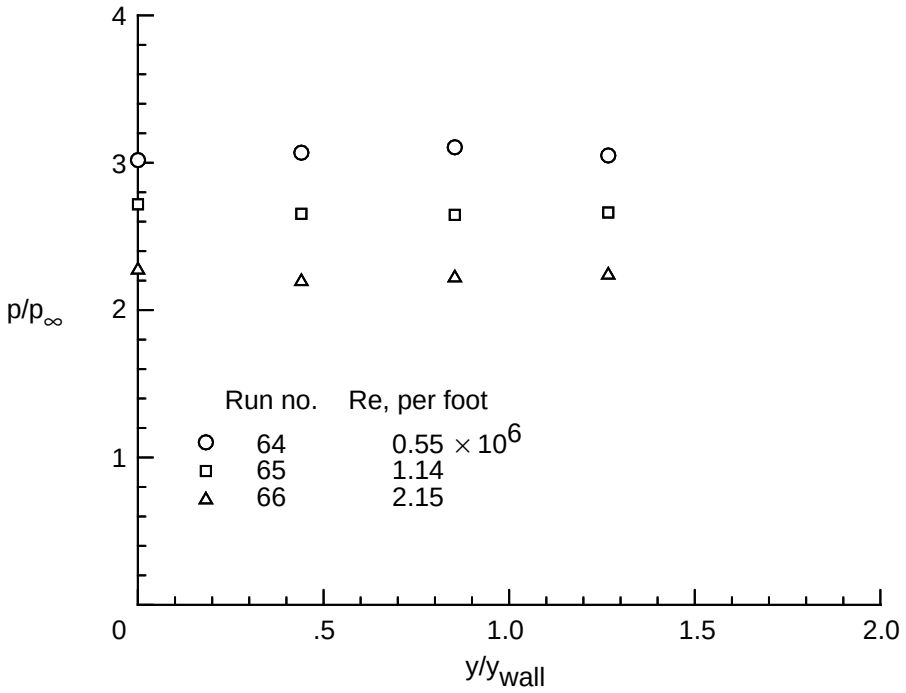

(b) Baseplate pressures. $x'/T_{x'} = -0.8412$.

Figure 19. Reynolds number effects on pressure distributions. CR = 3, 0 percent cowl.

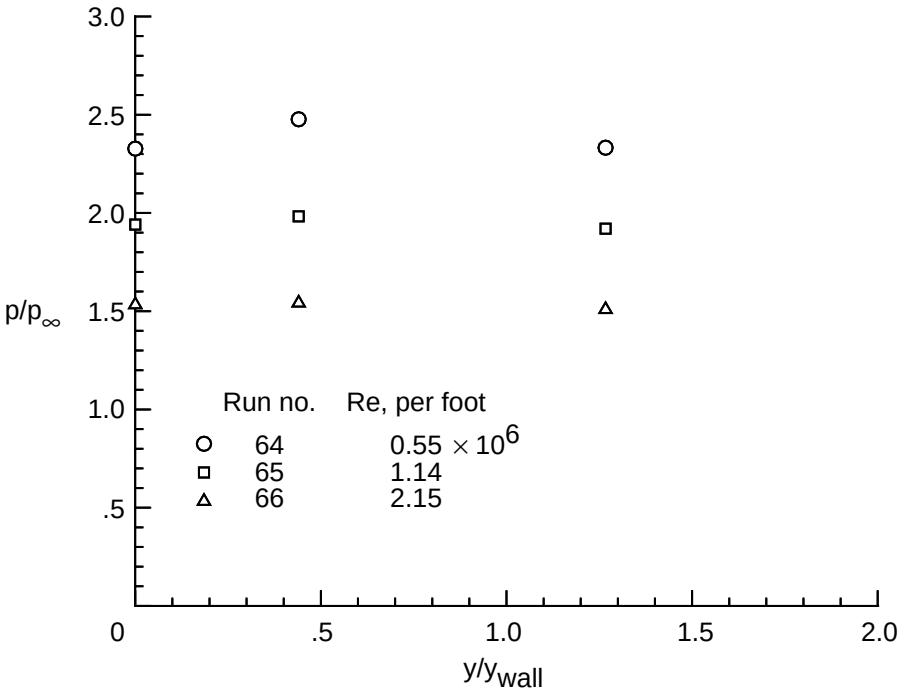

(c) Baseplate pressures. $x'/T_{x'} = -0.5258$.

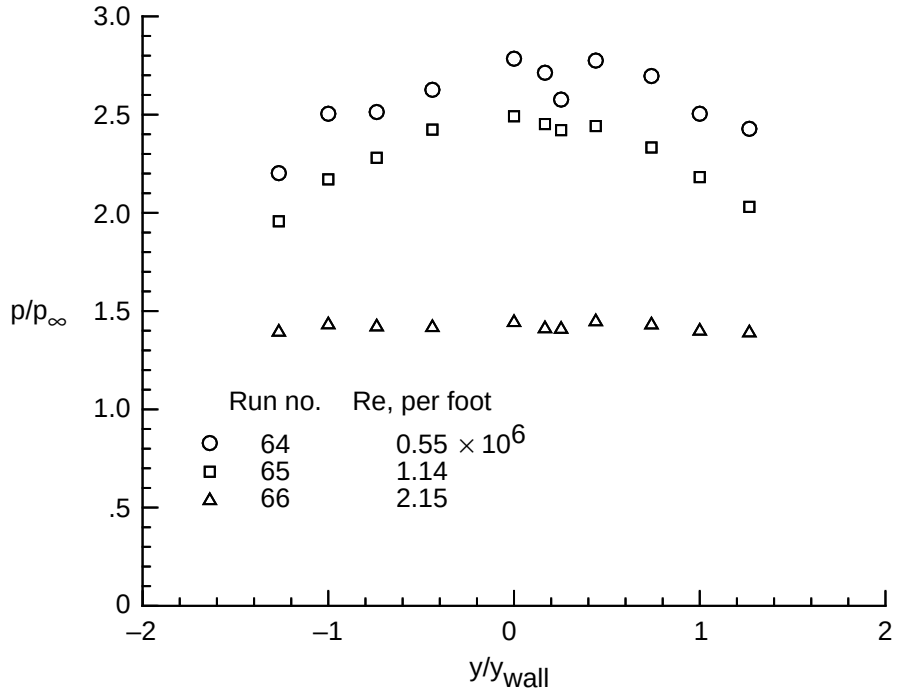

(d) Baseplate pressures. $x'/T_{x'} = -0.1052$.

Figure 19. Continued.

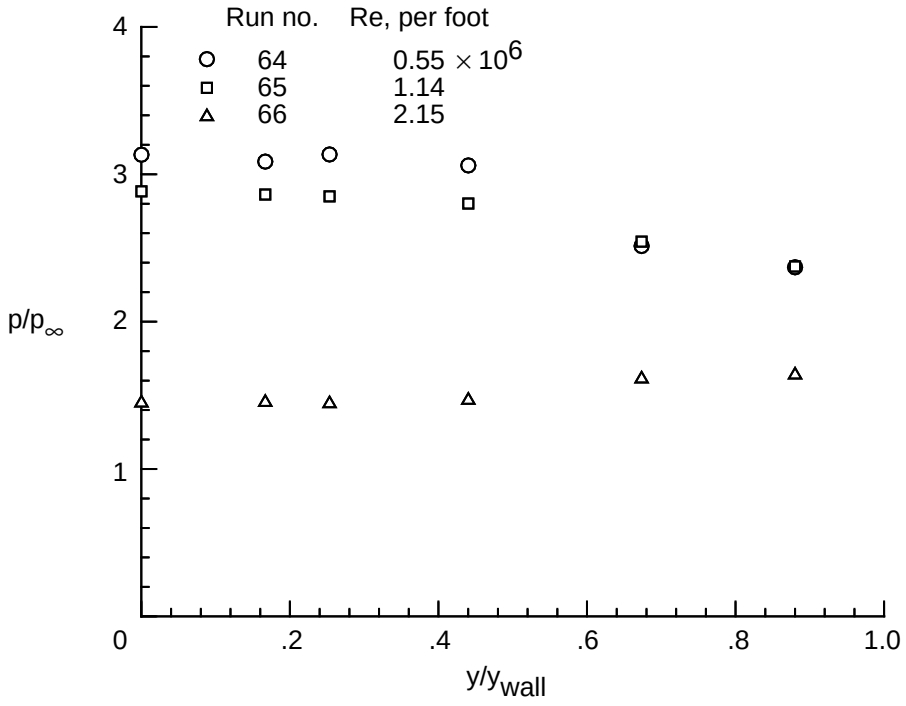

(e) Baseplate pressures. $x'/T_{x'} = 0$.

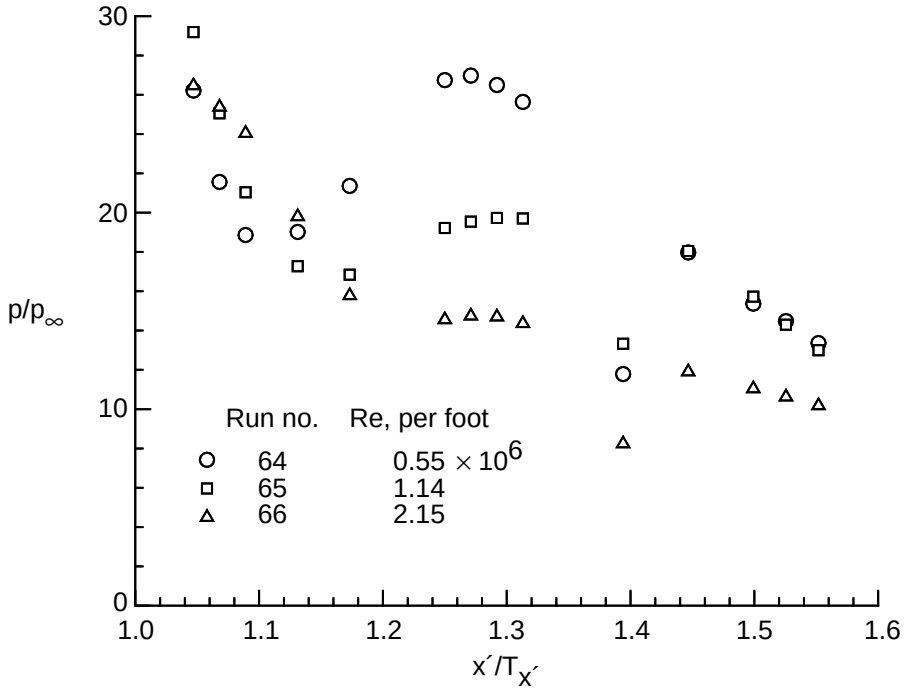

(f) Cowl pressures.

Figure 19. Continued.

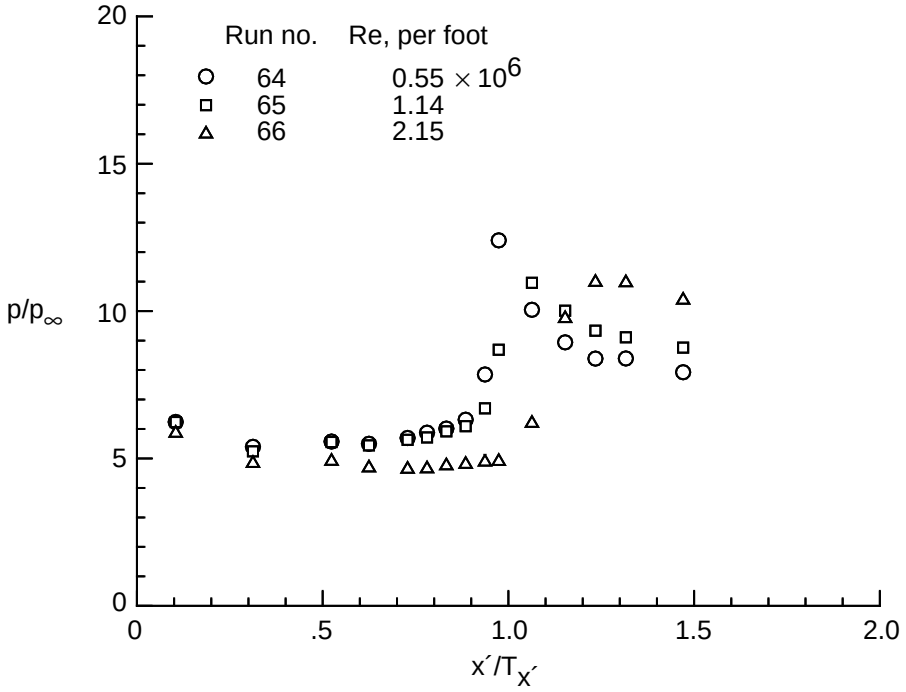

(g) Sidewall centerline pressures. $Z/H = 0.5$.

Figure 19. Concluded.

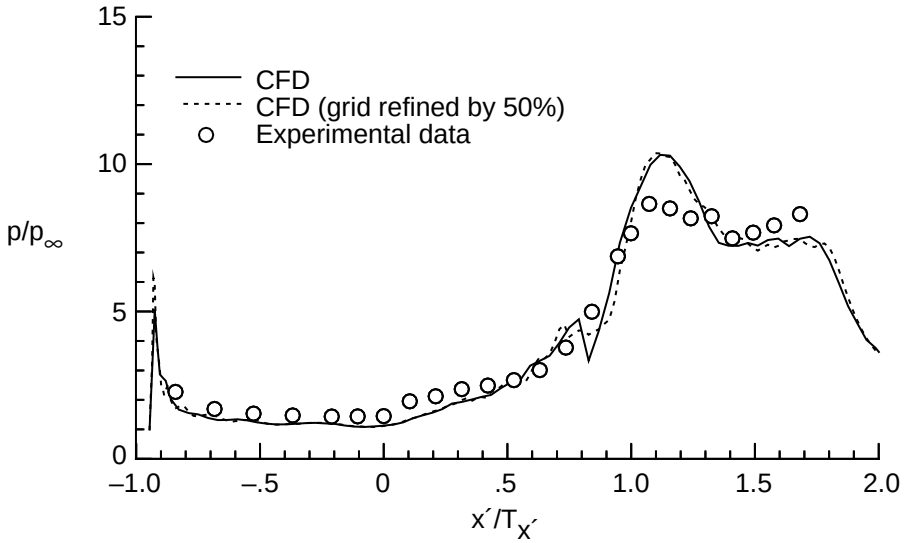

(a) Baseplate centerline.

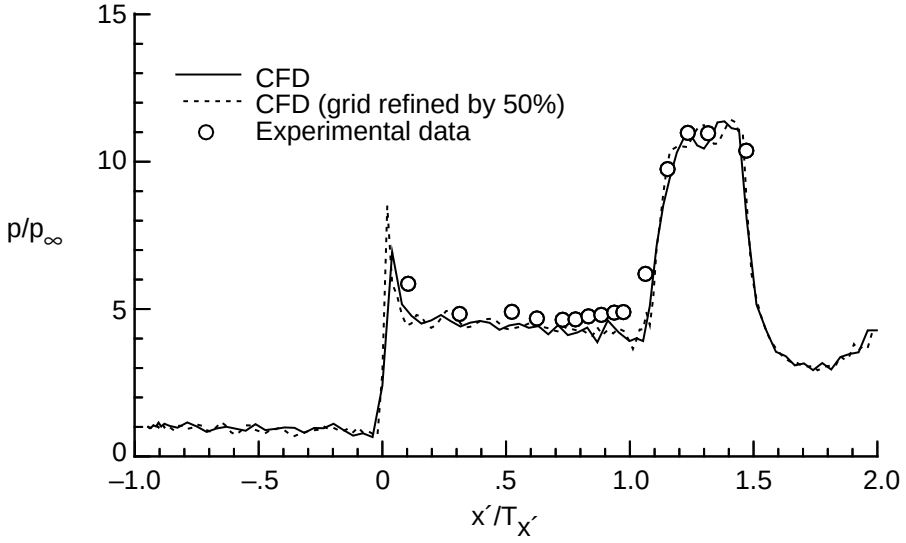

(b) Sidewall centerline.

Figure 20. CFD and experimental pressure distributions. CR = 3; Re = 2.15×10^6 per foot; 0 percent cowl.

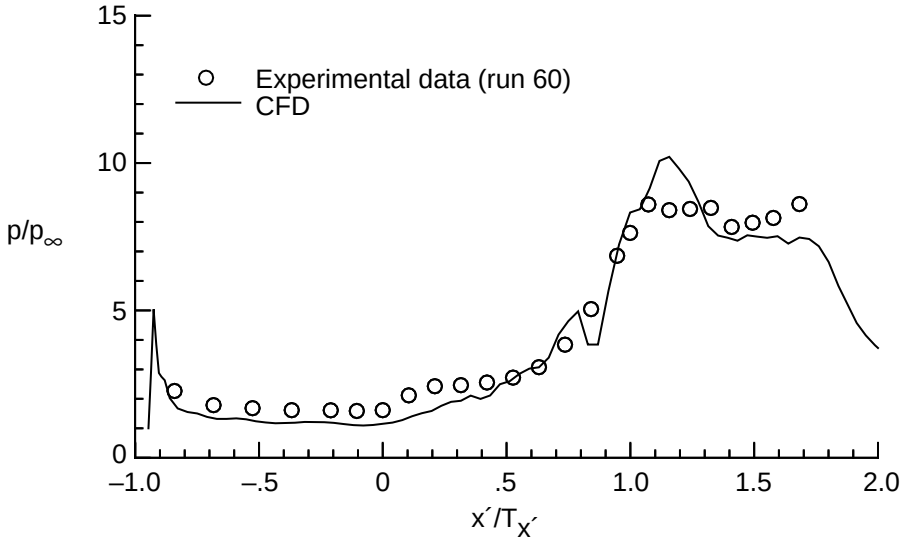

(a) Centerline pressures.

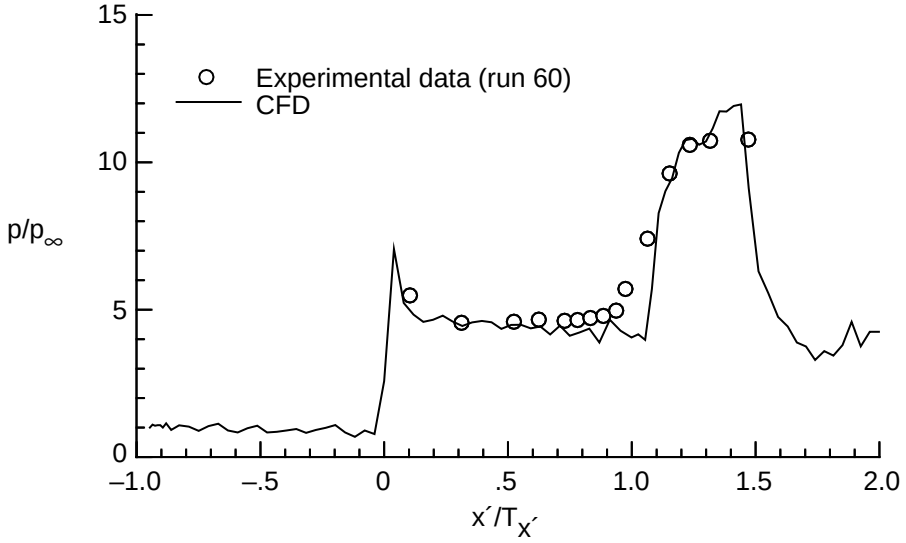

(b) Sidewall centerline pressures.

Figure 21. CFD and experimental pressure distributions. CR = 3; Re = 2.15×10^6 per foot; 50 percent cowl.

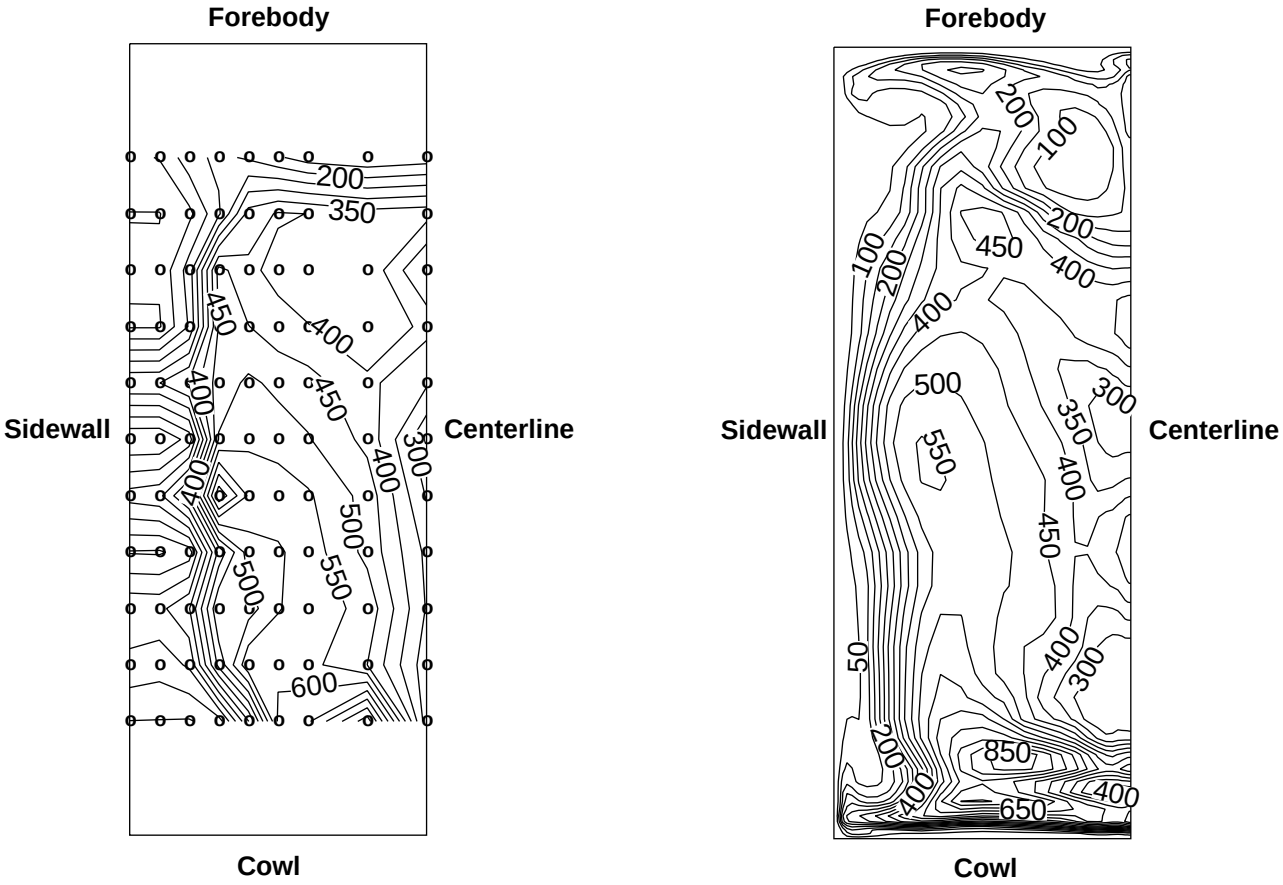

(a) Measured. Run 73.

(b) Computed.

Figure 22. $p_{t,2}/p_\infty$ exit plane contours. CR = 3; Re = 2.15×10^6 per foot; 0 percent cowl; lateral scale expanded by factor of 3.

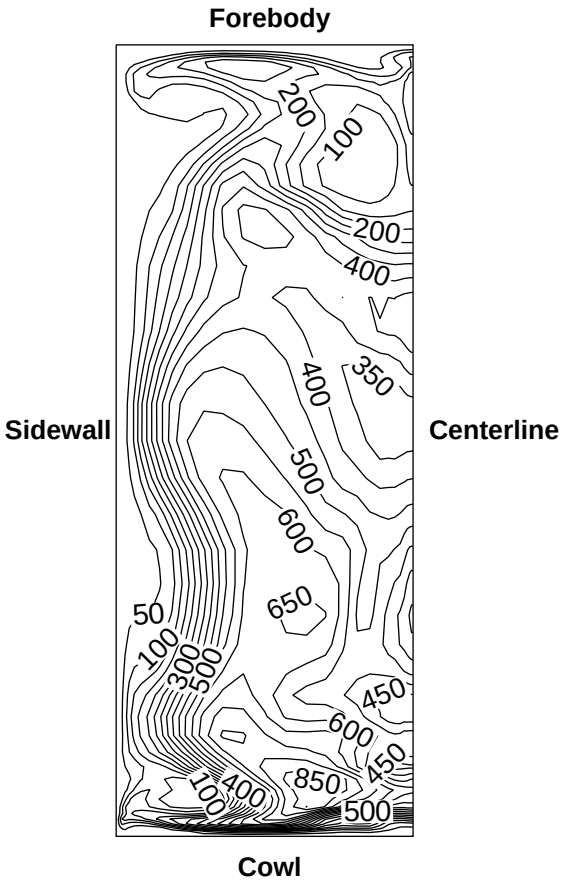

Figure 23. Computed $p_{t,2}/p_\infty$ exit plane contours. CR = 3; Re = 2.15×10^6 per foot; 50 percent cowl. Lateral scale expanded by factor of 3.

REPORT DOCUMENTATION PAGE

Form Approved
OMB No. 0704-0188

1. AGENCY USE ONLY *(Leave blank)*	2. REPORT DATE	3. REPORT TYPE AND DATES COVERED
	January 1995	Technical Paper

4. TITLE AND SUBTITLE
Internal Aerodynamics of a Generic Three-Dimensional Scramjet Inlet at Mach 10

5. FUNDING NUMBERS
WU 506-40-41-02

6. AUTHOR(S)
Scott D. Holland

7. PERFORMING ORGANIZATION NAME(S) AND ADDRESS(ES)
NASA Langley Research Center
Hampton, VA 23681-0001

8. PERFORMING ORGANIZATION REPORT NUMBER
L-17347

9. SPONSORING/MONITORING AGENCY NAME(S) AND ADDRESS(ES)
National Aeronautics and Space Administration
Washington, DC 20546-0001

10. SPONSORING/MONITORING AGENCY REPORT NUMBER
NASA TP-3476

11. SUPPLEMENTARY NOTES

12a. DISTRIBUTION/AVAILABILITY STATEMENT
Unclassified–Unlimited
Subject Category 34
Availability: NASA CASI (301) 621-0390

12b. DISTRIBUTION CODE

13. ABSTRACT *(Maximum 200 words)*

A combined computational and experimental parametric study of the internal aerodynamics of a generic three-dimensional sidewall compression scramjet inlet configuration at Mach 10 has been performed. The study was designed to demonstrate the utility of computational fluid dynamics as a design tool in hypersonic inlet flow fields, to provide a detailed account of the nature and structure of the internal flow interactions, and to provide a comprehensive surface property and flow field database to determine the effects of contraction ratio, cowl position, and Reynolds number on the performance of a hypersonic scramjet inlet configuration. The work proceeded in several phases: the initial inviscid assessment of the internal shock structure, the preliminary computational parametric study, the coupling of the optimized configuration with the physical limitations of the facility, the wind tunnel blockage assessment, and the computational and experimental parametric study of the final configuration. Good agreement between computation and experimentation was observed in the magnitude and location of the interactions, particularly for weakly interacting flow fields. Large-scale forward separations resulted when the interaction strength was increased by increasing the contraction ratio or decreasing the Reynolds number.

14. SUBJECT TERMS	15. NUMBER OF PAGES
Hypersonics; Inlets; Computational fluid dynamics (CFD); Shock interactions	54
	16. PRICE CODE: A04

17. SECURITY CLASSIFICATION OF REPORT	18. SECURITY CLASSIFICATION OF THIS PAGE	19. SECURITY CLASSIFICATION OF ABSTRACT	20. LIMITATION OF ABSTRACT
Unclassified	Unclassified	Unclassified	